Tuning Diblock Copolymer Particle Packing Symmetry with Variable Molecular Weight Core-Homopolymer

Andreas J. Mueller,† Aaron P. Lindsay,† Ashish Jayaraman,† Steven Weigand,#

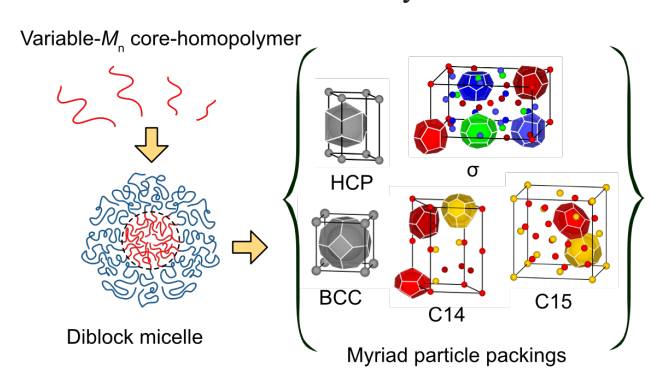
Timothy P. Lodge, †,‡ Mahesh K. Mahanthappa, †,* and Frank S. Bates †,*

[†] Department of Chemical Engineering and Materials Science and [‡]Department of Chemistry, University of Minnesota, Minnesota, Minnesota 55455

[#] DND-CAT, Advanced Photon Source, 9700 South Cass Ave, Argonne, Illinois 60439-4857

Corresponding Authors: <u>bates001@umn.edu</u>, <u>maheshkm@umn.edu</u>

For Table of Contents use only



ABSTRACT

We report the sensitivity of diblock copolymer particle packing symmetry to the ratio $\alpha = N_{\text{homo}}/N_{\text{core}}$, where N_{homo} and N_{core} are the respective homopolymer and core block degrees of polymerization. Three poly(ethylene oxide)-*b*-poly(2-ethylhexyl acrylate) (**OA**) diblock copolymers with **O** volume fractions f_0 = 0.15, 0.16, and 0.20 were blended with **O** homopolymers characterized by α = 0.23, 0.42, 0.80, and 1.00. SAXS revealed rich phase behaviors as a function of α , the overall particle core volume fraction (f_{core}), and temperature. BCC, HCP and Frank-Kasper phases σ , C14, C15, and a dodecagonal quasicrystal, were identified. A 'dry-brush' homopolymer distribution (α = 0.80 and 1.00) favors C14 and C15 phases, and macrophase separation at high homopolymer loadings. 'Wet-brush' homopolymer distributions in the particle cores (α = 0.42) lead to narrow σ or C15 windows and cylinders at greater **O** concentrations. Solvent-like swelling (α = 0.23) favors widespread σ phase formation.

INTRODUCTION

The emergence of complex micelle packings in self-assembling micellar materials represents a remarkable intersection between the fields of soft matter, metallurgy, and fundamental geometry. These low-symmetry structures, which are tetrahedral close-packings (TCPs) of particles, were originally conceived by Frank and Kasper to rationalize the remarkable breadth of transition metal alloy structures. 1,2 Almost 30 years later, TCPs surfaced as essential motifs in the last great shift in crystallography: the discovery of aperiodically ordered quasicrystals that display forbidden rotational symmetries (e.g., 12fold, etc.) without long-range translational symmetry. Recently, multiple Frank-Kasper (FK) phases and quasicrystals have emerged in micelle-forming soft materials, including lyotropic liquid crystals (LLCs) of minimally hydrated surfactants, 4-8 thermotropic dendrimers, 9-11 giant shape amphiphiles, 12-15 and block copolymers. 16,17 Comprising two chemically distinct homopolymers covalently linked end to end, linear diblock polymers are amongst the simplest molecules displaying this remarkable behavior. Historically, neat diblock copolymer melts were considered limited to the following phase progression with increasing volume asymmetry: lamellae (LAM) \rightarrow double gyroid (GYR) \rightarrow hexagonally-packed cylinders (HEXc) → body-centered cubic (BCC) sphere packing. Over the last 20 years, this phase sequence has been augmented with close-packed (FCC or HCP) micelle phases¹⁸⁻²⁰ and the Fddd network.^{21,22} Relatively recent discoveries of equilibrium FK σ and metastable C14, C15, and dodecagonal quasicrystal (DDQC) phases in poly(isoprene)-block-poly(rac-lactide) diblock melts, ^{23–25} followed by an equilibrium A15 phase in poly(dodecyl acrylate)-block-poly(rac-lactide), ²⁶ triggered a re-evaluation of our understanding of diblock phase behavior with renewed focus on how nuances in chain packing impact mesophase symmetry.

Whereas high-symmetry BCC, HCP, or FCC lattices each possess a single symmetry-equivalent local coordination environment arising from a mixture of tetrahedral and octahedral clusters of particles, FK phases exhibit combinations of 12-fold, and 14-, 15- and/or 16-fold coordination environments in order to tessellate space with a purely (albeit distorted) tetrahedral construction. Consequently, FK phases require the formation of multiple particle shapes and sizes within the unit cell, e.g., the FK σ phase

contains 30 particles of 5 distinct symmetry-equivalent types.^{27–30} Both the canonical BCC and HCP lattices, along with the FK σ , C14, and C15 phases and a schematic of a diblock copolymer micelle, are illustrated in Figure 1.

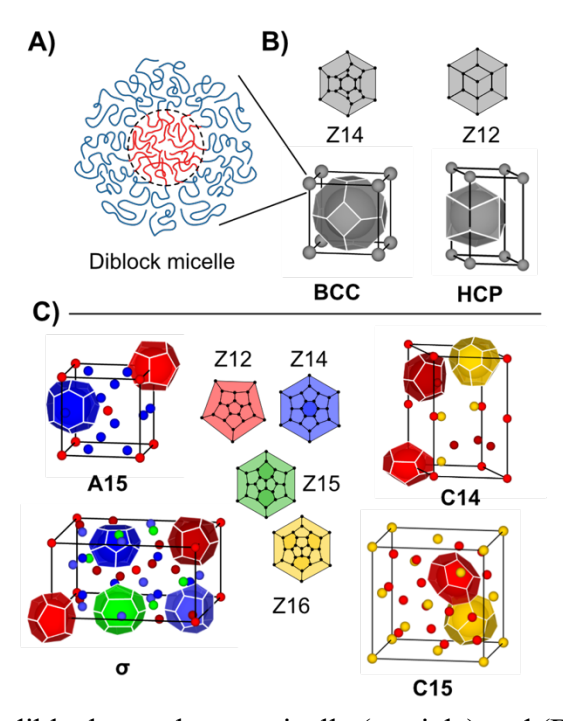


Figure 1: (A) Illustration of a diblock copolymer micelle (particle) and (B-C) the associated crystal structures reported in this work. The crystalline unit cells are each accompanied by planar graphs of the polyhedral Wigner-Seitz cells. Different shades of the same color in (C) represent different particle volumes but with the same geometric motif.

The spontaneous particle volume asymmetry found in FK phases that arises from a nominally single component liquid hinges on local particle shape optimization. For low core volume compositions (f_{core}), the stable BCC phase minimizes corona-corona repulsion between neighboring particles; in other words, minimal packing frustration is associated with filling the truncated cuboctahedron polyhedral coordination cells in BCC with diblock chains.³¹ For larger f_{core} , surface area-minimizing FK phases become favored as polyhedral particle corona faceting is transmitted onto the core/corona interfaces, resulting in excess interfacial area.^{27–30} This connection between TCPs of hard spheres and surface tension minimization in space-filling polyhedra, which was originally established in optimal dry foam structures,³² is apparent from the planar graphs ("Schlegel diagrams") associated with particles in the different lattices in Figures 1B and 1C. Note that FK phases comprise polyhedra having only pentagonal

and hexagonal faces, which generate favorable angles of intersection with neighboring particles that minimize surface tension. This contrasts the BCC and HCP packings, in which particles have less favored square (BCC) or trapezoidal facets (HCP).

FK phase formation in neat diblock melts has largely been achieved both in theory^{26,33} and in experiments, 26,34 by tuning the conformational asymmetry $\varepsilon = (b_{corona}/b_{core})^2 > 1$ where b_i is the statistical segment length of block i. This asymmetry in the space-filling characteristics of the segments manifests as stiffening of the particle coronae relative to the cores, driving interfacial curvature towards the core domains to stabilize particle morphologies at larger f_{core} values. In narrow dispersity diblocks, the equilibrium BCC $\rightarrow \sigma \rightarrow A15 \rightarrow HEX_c$ phase progression has been documented with increasing f_{core} . Other reports have demonstrated similar effects through architectural asymmetry, f_{core} as in coil-brush architectures and miktoarm stars. f_{core} However, investigations of FK phases of diblock melts have been limited to systems with low degrees of polymerization (f_{core}) and access to presumably metastable C14 and C15 phases therein requires specific thermal processing pathways.

Recent efforts have shifted to accessing complex particle packings by blending. Self-consistent field theory (SCFT) calculations indicate that judiciously designed binary diblock copolymer blends stabilize FK phases, even though the pure blend constituents form only BCC, HEX, GYR, and LAM.^{42,43} This prediction was experimentally verified by identification of σ , A15, C14, and DDQC phases in binary blends of polystyrene-*block*-poly(1,4-butadiene) (**SB**) diblocks.^{44–46} Blends of poly(1,4-butadiene)-*block*-poly(ε -caprolactone) with poly(1,4-butadiene) (**B**) core homopolymer were also found to stabilize the σ phase.^{47,48} In minimally hydrated micelles of small molecule ionic surfactants swollen with an oil isostructural with the surfactant tails, Mahanthappa and coworkers discovered a strong propensity to form C14 and C15 Laves phases.^{49,50} Our translation of this concept to blends of **SB** and core-miscible **B**' homopolymer produced the progression of phases BCC $\rightarrow \sigma \rightarrow$ C14 \rightarrow C15 \rightarrow (C15 + homopolymer), on changing homopolymer concentration and temperature.⁵¹ Related experimental reports of homopolymer-swollen particle cores stabilizing the C15 phase,^{52,53} coupled with its occurrence in salt-doped ternary blends,⁵⁴ bolster these findings. These investigations collectively suggest that diblock

copolymer-based blends offer a unique opportunity to extract molecular and geometric design principles for accessing these nearly thermodynamically degenerate particle packings. Core-homopolymer/diblock copolymer blends are especially attractive for assessing the geometric features underpinning particle size variations in these soft FK phases.

While the A15 phase comprises particles with 12-fold and 14-fold coordination, and the σ phase is characterized by 12-fold, 14-fold, and 15-fold coordination environments, the C14 and C15 Laves phases contain only the smallest 12-fold and largest 16-fold coordination polyhedra. Accordingly, Laves phases are characterized by particle volume variations $\Delta V/V_{\rm average} \approx 20\%$ based on idealized Voronoi tessellations, 25 and a newer theory suggests that $\Delta V/V_{\text{average}} \approx 30\%$. The increased stability of FK phases in core-homopolymer/diblock blends, with a proclivity for Laves phase formation, has been rationalized in terms of classical dry- versus wet-brush homopolymer localization in the particle cores. 55–58 FK phaseforming blends designed with a homopolymer of the same molecular weight as that of the diblock core apparently drives homopolymer localization at the particle centers with preservation of high interfacial curvature of the compositionally asymmetric diblocks to high f_{core} . Since the homopolymer resides at the particle center, the core segment must no longer stretch to fill that space thereby relieving the packing frustration associated with large particle volume variations in C14 and C15. Subsequent theoretical studies validated this reasoning. ^{59,60} In the wet-brush limit ($\alpha \lesssim 0.6$), core homopolymer addition instead drives a transition away from particle phases to hexagonally-packed cylinders due to an increase in the interfacial area per diblock copolymer chain.⁵¹

These observations raise the question of whether the core-homopolymer distribution within the particle cores, affected by the molecular weight of the homopolymer additive (i.e., α), can alone dictate particle packing lattice symmetry. To explore this question, we blended conformationally asymmetric ($\varepsilon = bo^2/b_A^2 \approx 3.5^{61}$), particle-forming poly(ethylene oxide)-block-poly(2-ethylhexyl acrylate) (**OA**) diblock copolymers having varied core-polyethylene oxide (**O**) volume fractions $f_O = 0.15$ -0.20 with each of four **O** homopolymers of varied molecular weights spanning $0.18 \le \alpha \le 1.00$, where $\alpha = N_{\text{homo}}/N_{\text{core}}$ and N_{homo} and N_{core} are the respective **O** homopolymer and **O** block degrees of polymerization. These results

demonstrate remarkably sensitivity of the packing symmetry to variations in the particle core molecular configuration.

MATERIALS and METHODS

Synthetic and molecular characterization methods employed to produce the polymers investigated in this study are described in the Supporting Information, along with descriptions of the small-angle X-ray scattering (SAXS) experiments and related data interpretation.

RESULTS

A series of model **OA** diblock copolymers was synthesized by a previously reported route.⁶¹ Briefly, three **OA** diblocks were synthesized by atom transfer radical polymerization (ATRP) of 2-ethylhexyl acrylate (2-EHA) from an α -isobutyryl-**O** macroinitiator ($M_{n,0} \approx 2,000$ g/mol) to yield the three diblock compositions $f_0 = 0.15, 0.16$, and 0.20. Henceforth, these samples are referred to as **OAXX**, with 'XX' denoting the f_0 value. Each of these diblocks was blended with each of four commercially available **O** homopolymers, resulting in blends with $\alpha = 0.23, 0.42, 0.80$ and 1.0, spanning the expected wet-brush behavior ($\alpha = 0.42, 0.23$) through the dry-brush behavior ($\alpha = 1.0$) with an intermediate case ($\alpha = 0.80$). These homopolymers are designated **O-YY**, with 'YY' referring to 100α based on the nominal $M_{n,0} = 2,000$ g/mol of the common **O** segment in each diblock. Accordingly, the four homopolymers are denoted **O-23**, **O-42**, **O-80**, and **O-100**. Characterization data for each polymer sample are presented in Table 1. ¹H NMR spectroscopy, differential scanning calorimetry (DSC), size-exclusion chromatography (SEC), and matrix-assisted laser desorption/ionization mass spectrometry (MALDI) data for each of these polymers with chemical synthesis and sample preparation details are provided in the Supporting Information and in Figures S1-4.

Blend samples were prepared by combining measured amounts of benzene solutions with known concentrations of homopolymer or diblock copolymer, followed by freeze-drying to remove the solvent. Freeze-dried blend samples were then sealed under argon into aluminum TZero DSC pans (DSC Consumables, Austin, MN; 50 mg per pan) prior to thermal annealing. Morphological assignments were made by in-situ variable temperature synchrotron small-angle X-ray scattering (SAXS) experiments

performed at the Sector 5-ID-D or Sector 12-ID-B beamlines at the Advanced Photon Source (Argonne, IL). Two-dimensional SAXS patterns were azimuthally averaged to the one-dimensional form of intensity versus scattering wavevector magnitude $|q| = q = 4\pi\lambda^{-1}\sin(\theta/2)$, where $\lambda = 0.729$ and 0.886 Å were the incident radiation wavelengths (Sectors 5-ID-D and 12-ID-B, respectively) and θ is the scattering angle.

Table 1. Molecular Characteristics							
Entry ^a	$M_{ m n,O}{}^b$	$M_{\mathrm{n,A}}{}^{b}$	N^c	f_0^d	\mathcal{D}^e	$T_{\mathrm{m,O}}^{f}$	Schematic ^g
OA15	1,950	9,750	178	0.146	1.09	37 °C	~~~~~
OA16	1,950	9,000	166	0.15_{6}	1.11	39 °C	~~~~
OA20	2,100	7,220	141	0.19_{9}	1.10	38 °C	~~~~
O-23	440	-	6	-	1.08	5.7 °C	$\sim \alpha = 0.18$
O-42	810	-	11	-	1.06	21 °C	\sim $\alpha = 0.42$
O-80	1,560	-	21	-	1.02	47 °C	$\sim \alpha = 0.80$
O-100	1,950	-	27	-	1.04	53 °C	$\alpha = 1.00$

^a Samples are named **OAXX** with "XX" specifying the volume fraction of the poly(ethylene oxide) block. For **OYY**, "YY" refers to 100α . ^b Number-average molar mass (g/mol) reported from ¹H NMR end group analysis. ^c Degree of polymerization relative to the 118 ų reference volume and homopolymer densities of $\rho_0 = 1.064^{62}$ and $\rho_A = 0.902.^{63}$ ^d Volume fraction of the **O** block calculated from ¹H NMR end-group analysis. ^e Molar mass dispersity determined via SEC with RI detection, using PS standards for **OA** diblocks or via MALDI for **O** homopolymer. ^f Melting point of the semicrystalline **O** segment from DSC. ^g Schematic depiction of each polymer molecule where the block lengths correspond to polymer backbone lengths. Red corresponds to PEO, blue to P(2-EHA). Homopolymers are labeled with blend α-values relative to any diblock.

Synchrotron SAXS experiments demonstrated that the neat **OA** diblocks each form only BCC phases above the **O** melting temperature ($T_{\rm m} = 37{\text -}39~{}^{\circ}\text{C}$) and prior to disordering between 60 and 80 ${}^{\circ}\text{C}$. The following sections detail how this simple phase behavior begets complexity on adding **O** homopolymer to the particle cores, and how the packing symmetry depends on the additive $M_{\rm n}$. All of these blends are parameterized by the volume fraction of homopolymer additive $\phi_{\rm O}$, and the overall **O** volume fraction in the melt $f_{\rm O,tot} = \phi_{\rm O'} + f_{\rm O}\phi_{\rm OA}$ (i.e., the combined homopolymer and diblock **O** fraction, with $\phi_{\rm OA} = 1 - \phi_{\rm O'}$, the fraction of **OA** diblock).

 $\alpha = 1$ *Blends.* We first considered **O-100/OA20** blends with $\alpha = 1$, for comparison to a previous study of **B'/SB** blends with comparable α and diblock composition $f_{core} \approx 0.20.^{51}$ SAXS analyses (Fig. 2A) demonstrate that the BCC phase of the neat **OA20** melt transforms into a structure with $P4_2/mnm$ space group symmetry, assigned to with a = 49.0 nm and c/a = 0.529, on adding $\phi_{O'} = 0.024$ homopolymer. Note that this σ phase competes with a metastable dodecagonal quasicrystal (DDQC) phase at T = 55 °C on heating (see Fig. S5) immediately after melting the semicrystalline state into a liquid-like packing (LLP),

analogous to a previous report.⁶¹ Increased **O-100** loadings of $\phi_{O'} = 0.047$ and 0.070 lead to formation of crystal structures exhibiting $P6_3/mmc$ and Fd3(-)m space group symmetries, assigned to the Laves C14 and C15 phases with a = 27.6 nm (c/a = 1.63) and a = 42.0 nm, respectively, at 55 °C on cooling. Fully indexed SAXS patterns for each of these structures are given in Figure S6. Close inspection of the C15 pattern reveals splitting of Bragg reflections, corresponding to a coexistence of two C15 lattices with slightly different lattice spacings (see Fig. S6B for the 2D image). This is likely a result of nonequilibrium particle sizes resulting from slow equilibration kinetics underpinning homopolymer and diblock redistribution between micelles, as has been reported for bulk diblock melts.⁶⁴ This effect appears to be confined to the C15-forming samples as $T_{\rm ODT}$ of these blends exceeds experimental limits (Fig. S7), preventing the facile mass exchange required to achieve uniformity in average micelle aggregation number and/or homopolymer loading within different C15 grains.

The full phase diagram for the **O-100/OA20** blend series presented in the bottom panel of Figure 2B in terms of $\phi_{O'}$ (bottom axis) and $f_{O,tot}$ (top axis) indicates the stability windows for BCC, σ , C14 and C15 phases at temperatures below T_{ODT} and above the onset of **O** block crystallization ($T_{m,OA20} = 38$ °C). This phase diagram shows that the blend order-disorder transition temperatures (T_{ODT}) increase significantly on addition of **O-100**, consistent with **O** localization in the particle cores. For $\phi_{O} \ge 0.07$ where the C15 phase forms, the $T_{ODT} > 120$ °C exceeds the maximum temperature accessed in the SAXS experiments.

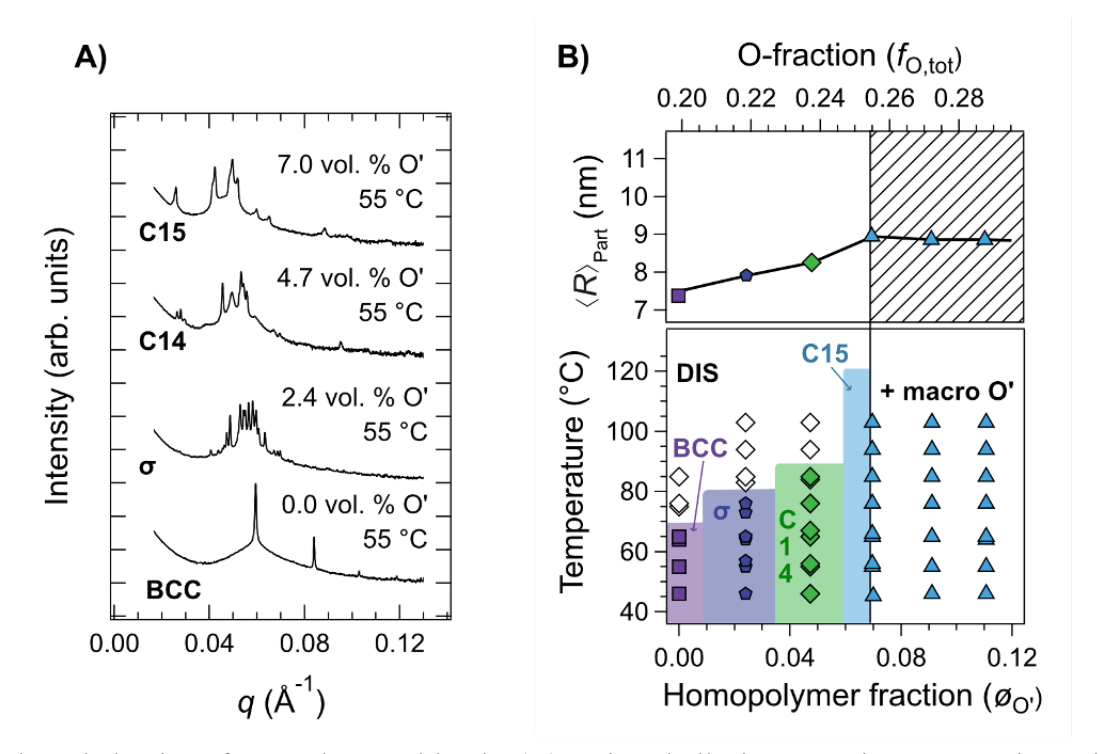


Figure 2: Phase behavior of **OA20/O-100** blends. (A) Azimuthally-integrated 1D-SAXS intensity profiles labeled with $\phi_{O'}$ acquired at 55 °C. (B) Temperature versus $\phi_{O'}$ (bottom *x*-axis) or f_O (top *x*-axis) phase portrait (*bottom panel*), and $\langle R \rangle_{part}$ versus $\phi_{O'}$ and $f_{O,tot}$ (top panel), at 55 °C. The hatched region in the top plot corresponds to the 'macro **O**' region in the phase portrait, which refers to **O** macrophase separation.

A comparison of the calculated average particle radius $\langle R \rangle_{part}$ at 55 °C as a function of increasing ϕ_O is presented in the top panel of Figure 2B. These calculations use the lattice parameters extracted from SAXS analyses, where $\langle R \rangle_{part}$ is the average total radius of a spherical particle (core and corona) based on the unit cell volume normalized by the number of particles per unit cell. The **O-100/O20** blend series is characterized by a monotonic increase in $\langle R \rangle_{part}$ with increasing ϕ_O until the formation of C15 at ϕ_O = 0.07, whereupon $\langle R \rangle_{part}$ plateaus. This transition was identified as the onset of macrophase separation, denoted by the hatched regions in Figure 2B, which extends into the full **O-100/OA20** blend phase diagram in the bottom panel of Figure 2B. The phase progression BCC $\rightarrow \sigma \rightarrow$ C14 \rightarrow C15 followed by macrophase separation reproduces findings in our earlier work on **SB/B'** blends⁵¹ and related theoretical predictions, ^{59,60,65} reinforcing the universality of this phase behavior across chemical systems with very different molecular weights and conformational asymmetries.

In order to explore the robustness of the blend phase sequence shown in Figure 2, we reduced the corecomposition of the BCC forming diblock to $f_0 = 0.15$ while maintaining $\alpha = 1$. SAXS traces and the phase diagram in Figure 3 shows that these O-100/OA15 blends are characterized by BCC \rightarrow C14 followed by macrophase separation at $\phi_{0'} \ge 0.055$. Absence of the σ phase prior to C14 formation may arise from insufficient composition resolution between BCC and C14, although Xie and Shi have reported a direct $BCC \rightarrow C14 \rightarrow (C14 + macrophase separated homopolymer)$ transition sequence in SCFT calculations involving a f = 0.15 diblock blended with $\alpha = 1$ homopolymer. 60 As evidenced by the saturation of $\langle R \rangle_{part}$ in Figure 3B, these O-100/OA15 blends also underscore the propensity for C14 formation coincident with macrophase separation. Close inspection of the peak intensity patterns of the C14 SAXS traces at $\phi_{0'}$ = 0.054 and 0.114 in Fig 3A reveals deviations in the intensity patterns expected for a well-developed C14 phase such as the $\phi_{0'} = 0.037$ blend in Fig 3A. The depression of the (101), (102), and (103) reflections of the C14 in these $\phi_{0'} = 0.054$ and 0.114 SAXS traces (red arrows Fig 3A) yield an intensity pattern intermediate between C14 and C15 (see Figure 2A and S6 for C15 comparison). However, a full indexing of the $\phi_{0} = 0.114$ pattern of Fig 3A indicates (see SI, Figure S8) the absence of any reflections unique to C15. Therefore, we assign this morphology as C14 albeit with structural defects such as stacking faults, which are known to cause plane-specific peak broadening and intensity loss by analogy to HCP packing. ⁶⁶ The formation of C14 in these low f_{core} OA15-based blends is reminiscent of the appearance of a metastable C14 phase in a σ-forming PI-PLA diblock copolymer melt subjected to deep thermal quenches from the disordered state. 25,42 Only a higher fcore PI-PLA diblock, which forms an equilibrium HEXc phase, displayed a C15 phase in related quenching experiments. Accordingly, these findings suggest that the sequence BCC $\rightarrow \sigma \rightarrow C14 \rightarrow C15$ may be limited to blends with a diblock possessing an already significant core-fraction ($f_{core} \approx 0.20$) and a smaller corona, and that the free energy landscape changes considerably for diblocks with lower f_{core} (i.e., a larger corona).

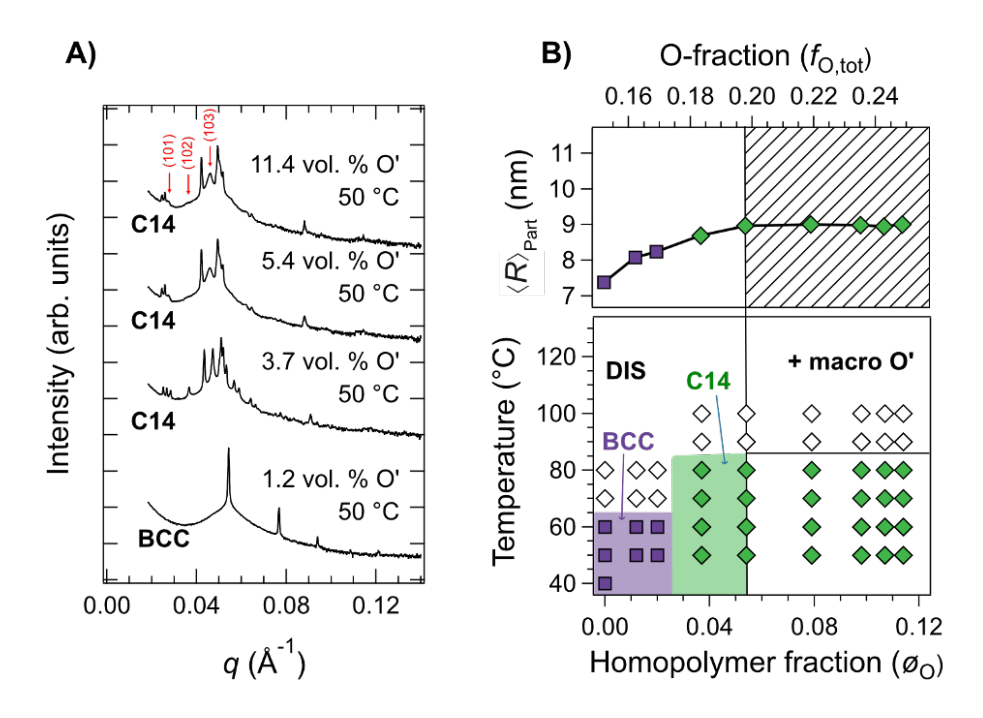


Figure 3: Phase behavior of **O-100/OA15** diblock/homopolymer blends. (A) Azimuthally-integrated 1D powder SAXS profiles labeled as a function of ϕ_0 at 50 °C. (B, *bottom panel*) Temperature versus ϕ_0 (bottom x-axis) or $f_{0,\text{tot}}$ (top x-axis) phase portrait of **O-100/OA15** blends and (B, *top panel*) the evolution of $\langle R \rangle_{\text{part}}$ with **O** addition at 60 °C. **O** macrophase separation occurs at $\phi_0 \geq 0.055$, denoted by the hatched regions in the top $\langle R \rangle_{\text{part}}$ plot and the 'macro O' region in the bottom phase portrait.

 α < 1 Blends Phase portraits and SAXS data for the **O-80/OA15** and **O-23/OA15** blends are shown in Figure 4. Mixing **O-80** with **OA15** leads to phase behavior resembling that of **O-100/OA15** blends: a BCC phase forms at low ϕ_O and C14 coexisting with a homopolymer-rich phase is observed at higher **O** loadings (Figure 4A). The degree of swelling is also very similar, as $\langle R \rangle_{part}$ swells from 7 nm to ~9 nm, with macrophase separation near $\phi_O = 0.05$ in both cases. However, **O-80/OA15** blends with intermediate **O** loadings $\phi_O = 0.02$ –0.03 somewhat surprisingly exhibit 1D-SAXS patterns that index to the P63/mmc space group (Figure 4B) indicative of hexagonally close-packed (HCP) particle packing (see Figure S9 for full indexing). This HCP phase appears to be favored at low temperatures, while BCC forms near T_{ODT} . As Fig. 4D demonstrates, the HCP phase forms after heating and cooling, suggesting an equilibrium HCP \rightarrow BCC \rightarrow DIS progression, which to our knowledge is unprecedented in block copolymers. Note that Jayaraman and Mahanthappa previously recorded such transitions in LLCs of ionic surfactants that form FK phases.⁷ For bulk diblock copolymer melts, close-packed structures are predicted to be

thermodynamically favorable very near $T_{\rm ODT}$, while BCC and possible FK phases dominate at stronger segregation. ^{19,67,68}

In fact, even the **O-100/OA15** blend with $\phi_{O'} = 0.012$ showed evidence of HCP order on cooling from the BCC state at T < 30 °C (see Figure S10), which lies outside the temperature range shown in Fig. 3. This low temperature HCP phase, with some additional (101) peak splitting suggestive of a C14 phase, is **metastable** and ultimately reverts to a disordered semicrystalline state at room temperature.

SAXS profiles for **O-80/OA15** blends with slightly higher $\phi_{O'} = 0.03$ –0.04 demonstrate these blends also form HCP phases, with additional features attributable BCC and C14. Accordingly, these points are marked as 'Coex' for phase coexistence in Fig. 4B. This window of phase coexistence may reflect slow ordering kinetics during thermal annealing, although the Gibbs Phase Rule anticipates equilibrium phase coexistence between regions of pure phases in binary mixtures.

Reducing $\alpha = 0.80$ to 0.23 did not trigger the expected transition to HEXc phases in the **O-23/OA15** blends. Instead, the region of stability of the HCP phase expanded to $0.015 \le \phi_{O'} \le 0.060$, with terminal swelling and the onset of **O** macrophase separation from the σ phase at $\phi_{O'} \ge 0.07$ as in Fig. 4C. The change in particle packing symmetry to σ at the boundary of macrophase separation is accompanied by an overall increase in particle size relative to the **O-100/OA15** and **O-80/OA15** blends, with $\langle R \rangle_{\text{part}} \approx 9.5$ nm as opposed to the dry-brush blends with maximal $\langle R \rangle_{\text{part}} \approx 9$ nm.

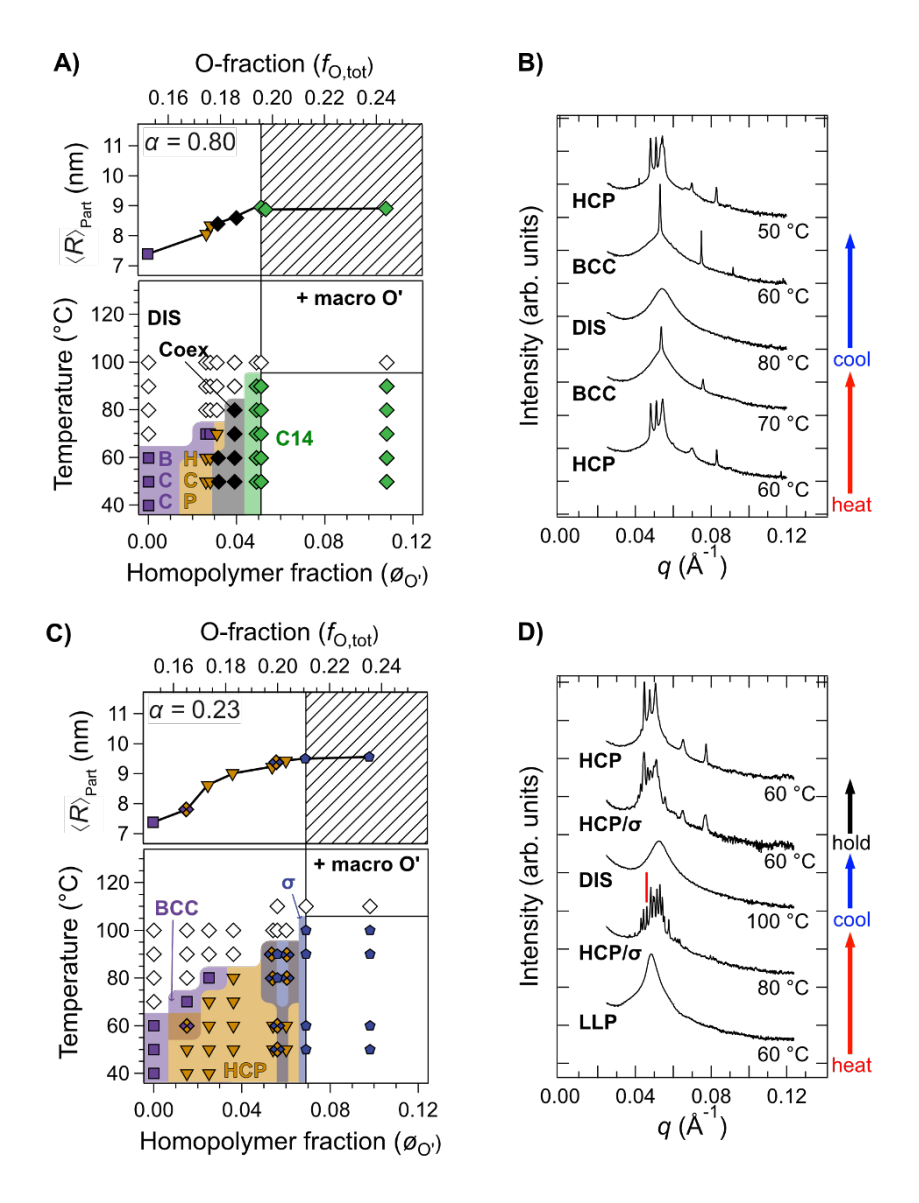


Figure 4: Temperature versus $\phi_{O'}$ (bottom x-axis) or $f_{O,tot}$ (top x-axis) phase diagrams and (top panel) $\langle R \rangle_{part}$ dependence on **O** loading at 60 °C for (A) **O-80/OA15** blends with (B) SAXS profiles of the **O-80/OA15** blend with $\phi_{O'} = 0.026$. (C) Phase portrait of **O-23/OA15** blends with (D)SAXS profiles of the **O-23/OA15** blend with $\phi_{O'} = 0.060$. The hatched regions in the top $\langle R \rangle_{part}$ plots of (A) and (C) correspond to the 'macro O'' regions in the bottom phase portraits of each panel, indicating the onset of macroscopic **O** phase separation.

This difference is likely due to an increase in interfacial area per diblock chain driven by the increased penetration of the low M_n homopolymer near the O/A interface as expected for wet brush homopolymers. Note that such a low- α homopolymer may act as a less preferential solvent that significantly partitions into the corona domains. However, the O-23/OA15 blends exhibit significant increases in T_{ODT} (Figure 4C) as with the O-100/OA15 and O-80/OA15 blends, consistent with homopolymer localization in the O core domains.

Inspection of the O-23/OA15 blend diagram (Figure 4C) reveals unique phase behavior around the HCP state that spans $0.01 < \phi_{O'} < 0.06$. When $\phi_{O'} < 0.03$, HCP and BCC respectively occur at low and high temperatures, as in O-80/OA15 at slightly higher homopolymer loadings. Figure 4D shows that a O-23/OA15 blend with $\phi_{O'} = 0.060$ forms a well-ordered σ phase at 80 °C on heating from the liquid-like packing state (LLP) at 60 °C after melting the ambient temperature equilibrium semicrystalline state (not shown). This σ phase formed at 80 °C exhibits one extra diffraction peak, marked by the red arrow in Figure 4D. Subsequent disordering and cooling of this structure reveals a coexistence between σ and HCP at 60 °C, which on annealing for 16 h matures into a pure HCP packing. This finding suggests that the additional Bragg peak found at 80 °C also corresponds to HCP. Once more, the apparent preference for HCP at higher segregation strengths (low temperatures) conflicts with our current understanding of the geometric principles governing the thermodynamics of diblock copolymer self-assembly: FK or BCC phases are favored in this segregation strength limit, depending on overall core domain volume fraction.

To probe the impact of overall core composition on the phase behavior documented in the **O/OA15** blends shown in Figure 4, additional **O-80/OA20** and **O-23/OA20** blends were prepared. Representative SAXS data and an experimental phase diagram for **O-80/OA20** blends are presented in Figures 5A and 5B, respectively. Pure **OA20** forms a BCC phase, which disorders at about 70 °C (see Figure 2). Addition of **O-80** homopolymer results in σ phase formation at $\phi_{O'} = 0.025$, which persists up to $T_{ODT} = 80$ °C (Figure 5B). A metastable dodecagonal quasicrystal (DDQC) phase is seen at $\phi_{O'} = 0.047$ up to 75 °C, where transformation to σ occurs nearly concurrently with disordering.

These blends terminate in C14/C15 coexistence with macrophase separation at $\phi_{O'} \ge 0.07$. Overall, the **O-80/OA20** blends closely mirror **O-100/OA20** blends (Fig. 2C) excepting the clean delineation of C14 and C15 in the latter. Also, note that the $\phi_{O'} = 0.047$ σ -forming blend exhibited kinetically limited ordering on heating from lower temperatures, hence the lack of data points at T < 75 °C (Figure 5B); no well-formed σ phase was observed during the heating and cooling ramps performed on this sample over the course of 12 h.

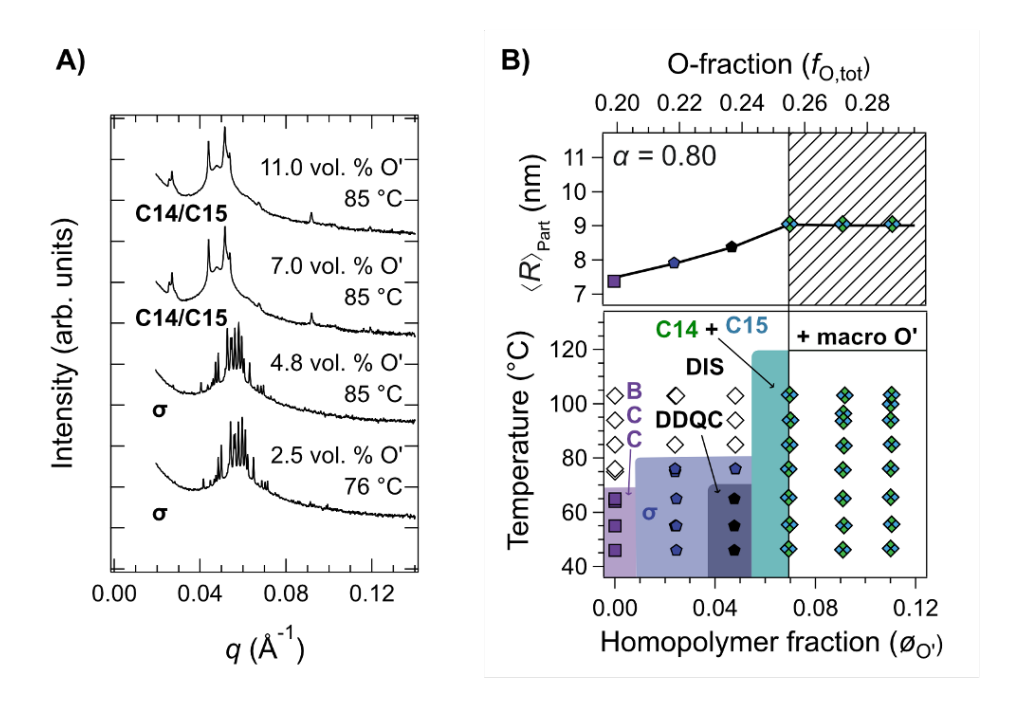


Figure 5: (A) SAXS profiles of **O-80/OA20** blends labelled with $\phi_{O'}$ and the annealing temperature. (B, *bottom panel*) Temperature versus $\phi_{O'}$ (bottom x-axis) or $f_{O,tot}$ (top x-axis) phase diagram of **O-80/OA20** blends and (*top panel*) $\langle R \rangle_{part}$ versus homopolymer loading at 55 °C. The hatched regions in the $\langle R \rangle_{part}$ plots correspond to the 'macro O'' regions in the bottom phase portraits of each panel, indicating the onset of macroscopic phase separation of excess **O-80** homopolymer.

Figure 6A displays the phase behavior of the wet-brush **O-23/OA20** blends for $0 \le \phi_{O'} < 0.4$. These blends display an expanded window of $\sigma/DDQC$, with continuous particle swelling up to $\phi_{O'} = 0.11$, at which point only a (presumably metastable) DDQC is observed over all experimentally probed temperatures, due to the strong segregation at $T \le T_{ODT}$.

At relatively high O-23 loadings, $0.13 \le \phi_{O'} \le 0.42$, the SAXS analyses suggest a Laves phase packing with short range order, labeled 'Lav.' in Figure 6B, possibly due to slow ordering kinetics at strong segregation. The broad peaks are consistent with Fd3(-)m symmetry associated with C15, making it possible to estimate $\langle R \rangle_{part}$ from these data along with the well-resolved BCC, σ , and DDQC at low $\phi_{O'}$ when T = 55 - 65 °C as in the top panel of Figure 6A. Whereas the other particle sizes saturate near $\langle R \rangle_{part} = 9-9.5$ nm in all of the other blends, these blends exhibit O swollen particles with $\langle R \rangle_{part} = 11$ nm. Furthermore, this saturation only occurs at $f_{O,core} = 0.40$, which is well beyond the expected composition for HEXc formation.

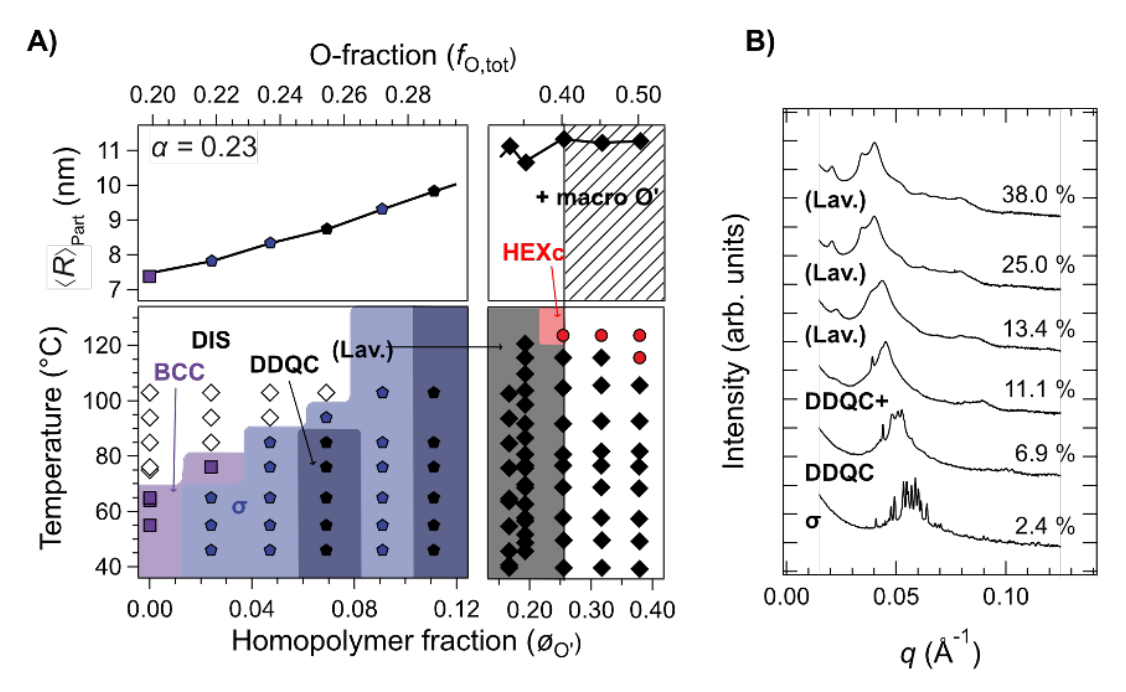


Figure 6: (A) Temperature versus $\phi_{\text{O'}}$ (bottom x-axis) or overall $f_{\text{O,tot}}$ (top x-axis) versus temperature phase portrait and (top panel) $\langle R \rangle_{\text{part}}$ versus homopolymer loading at 60 °C for **O-23/OA20** blends. (B) SAXS profiles of **O-23/OA20** blends at temperature T = 55-65 °C labeled with $\phi_{\text{O'}}$.

This suggests that some of the \mathbf{O} homopolymer in these blends partitions into the corona domains, rather than remaining exclusively in the particle cores. However, preferential core segregation of homopolymer rather than a uniform distribution in the microstructure is supported by T_{ODT} of these blends increasing with homopolymer loading. Distributing homopolymer between particle cores and coronas would be expected to produce a compatibilization effect, driving the blend T_{ODT} down rather than up.

A surprising result from the **O-23/OA20** blends (Figure 6) is that blends with $\phi_{O'} \ge 0.25$ transition to HEXc at high temperatures. As shown in Figure 7, heating from 111 to 124 °C transforms the LLP-like scattering into a distinctly HEXc pattern, which reverts to a Laves phase packing lacking long range order ('Lav.') on cooling to 78 °C. Based on the invariant particle radius over $0.25 < \phi_{O'} < 0.40$ at 55-65 °C (Fig. 6A), we infer the blends are macroscopically phase separated over this range of compositions with expulsion of **O** homopolymer from the ordered domains.

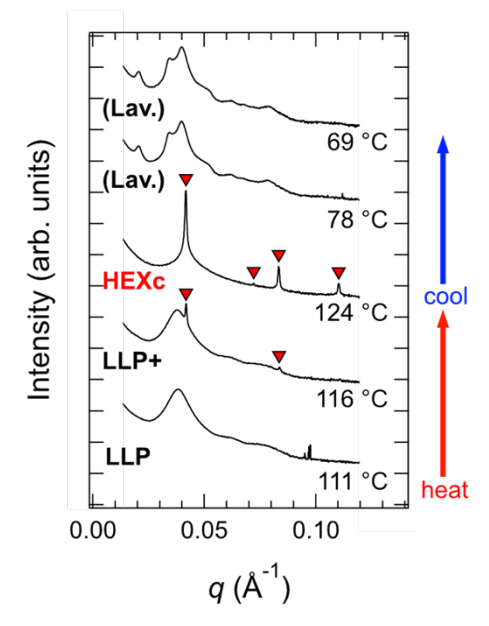


Figure 7: Variable temperature SAXS data for the **O-23/OA20** blend with $\phi_{O'} = 0.42$. Red triangles on selected traces indicate indexing to hexagonally packed cylinders (HEXc).

Finally, we prepared a set of O-42/OA20 and O-42/OA16 blends to bridge the wet and dry brush limits associated with the O-23 and O-80 additives. The OA16 diblock copolymer was synthesized as a surrogate for OA15, which was depleted during the initial studies. Figures 8 and 9 depict the phase behavior of the O-42/OA16 and O-42/OA20 blends, respectively, which each produce HEXc at homopolymer loadings of $\phi_{0'} > 0.05$, similar to the wet-brush behavior reported in a previous publication.⁵¹ However, a deviation from the direct BCC → HEXc progression was observed at intermediate $\phi_{O'}$ (Figure 8B). Temperature-dependent SAXS on the **O-42/OA16** blend with $\phi_{O'} = 0.055$ instead revealed a transition from HEXc to C15 on cooling, illustrated in Figure 8A. A similar competition between a high temperature HEXc phase and low temperature C15 was discussed in the context of the O-23/OA20 blends shown in Figure 6. A full indexing of the $\phi_{\rm O} = 0.055$ O-42/OA16 blend HEXc/C15 coexistence is given in Figure S11. The occurrence of a high temperature HEXc phase in corehomopolymer diblock blends conflicts with recently reported SCFT simulations, where HEXc is predicted to dominate at high segregation strengths (low temperature). 60 A full phase portrait for the **O-42/OA16** blends in the bottom panel of Figure 8B indicates a phase progression of BCC $\rightarrow \sigma \rightarrow C15 \rightarrow HEXc$. This tendency for FK phase formation at low homopolymer loadings for O-42 blends was also recovered in part in the **O-42/OA20** blends, evidenced by the SAXS traces in Figure 9A showing a well developed σ phase at $\phi_{O'} = 0.030$ that transforms into HEXc at at $\phi_{O'} = 0.070$. Note data for the $\phi_{O'} = 0.030$ blend were only collected on heating.

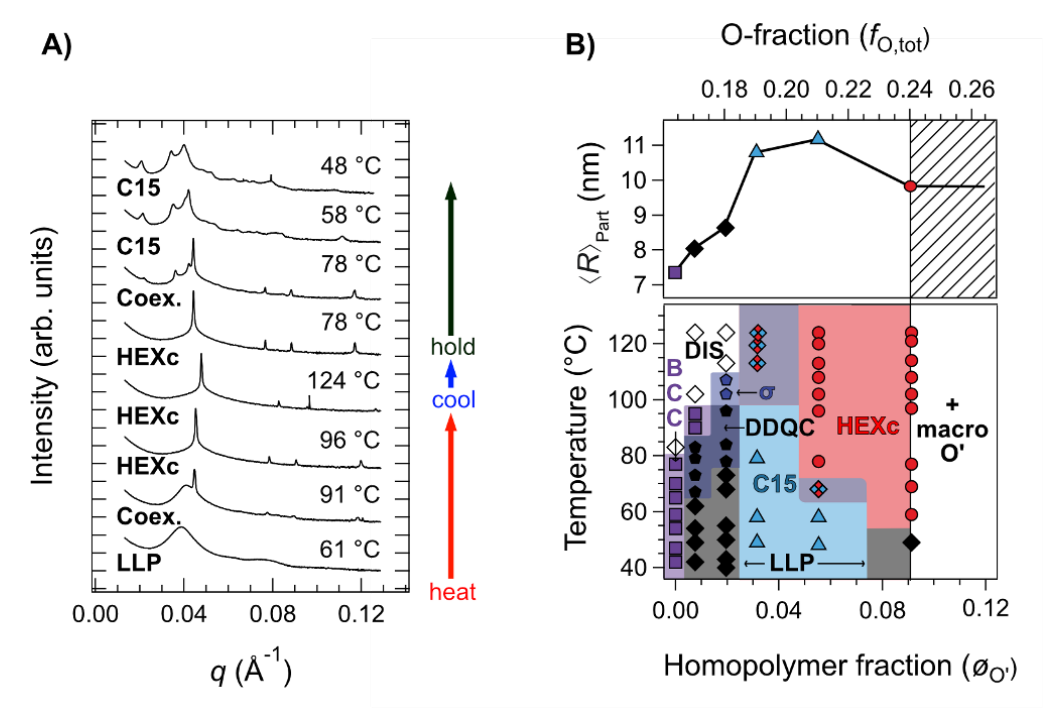


Figure 8: (A) Variable temperature synchrotron SAXS traces of the **O-42/OA16** blend with $\phi_{O'} = 0.055$. (B) Temperature versus $\phi_{O'}$ (bottom x-axis) or overall $f_{O,tot}$ (top x-axis) versus temperature phase portrait and (top panel) $\langle R \rangle_{part}$ versus homopolymer loading at 60 °C for **O-42/OA16** blends.

Conceivably due to the lower composition resolution of the **O-42/OA20** phase portrait in the bottom panel of Figure 9B, no C15 was observed between σ and HEXc in these blends. The σ phase in both **O-42/OA20** and **O-42/OA16** blends competes with metastable LLP or DDQC states at lower temperatures due to arrested interparticle mass exchange dynamics far below T_{ODT} .

Formation of cylinders in **O-42** blends was accompanied by a sharp increase in T_{ODT} , rising from below 80 °C for **OA16** and 70 °C for **OA20** to > 120 °C in each case. Macrophase separation of **O** from the HEXc morphology was observed in both cases, specifically at $\phi_{\text{O'}} \ge 0.055$ and $\phi_{\text{O'}} \ge 0.070$ in the **O-42/OA16** and O-42/OA20 blends respectively. Prior to the onset of HEXc formation, $\langle R \rangle_{\text{part}}$ in the **O-42/OA16** blends rapidly increases to just over $\langle R \rangle_{\text{part}} = 11$ nm.

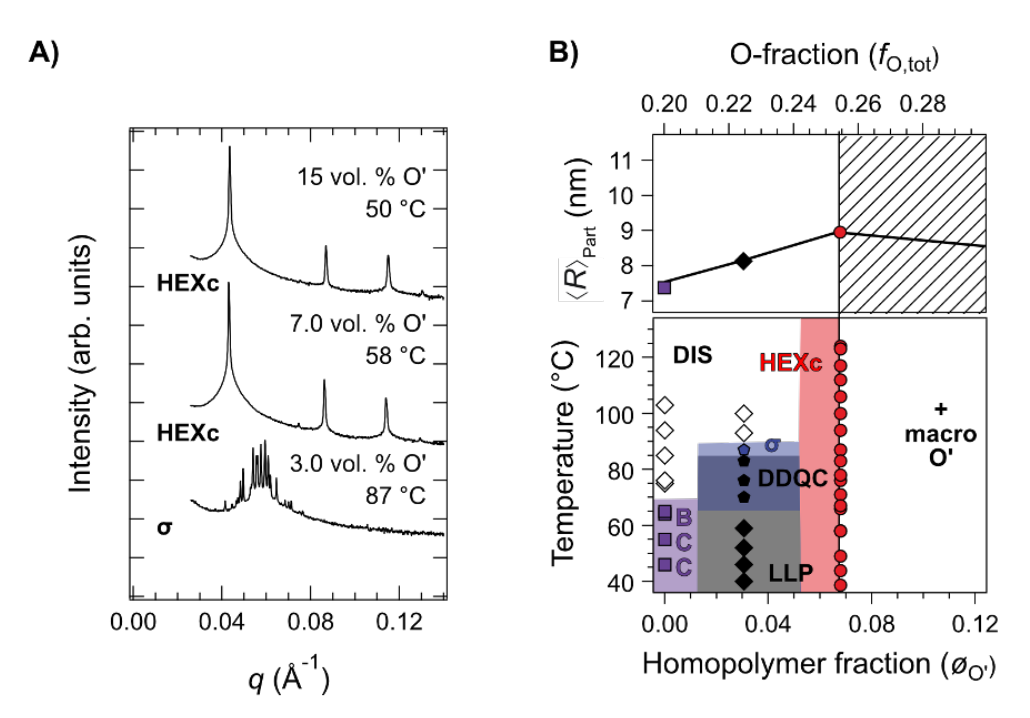


Figure 9: Phase behavior of **O-42/OA20** blends. (A) Selection of variable temperature synchrotron SAXS traces labeled with annealing temperature and homopolymer loading. (B)Temperature versus $\phi_{\text{O'}}$ (bottom x-axis) or overall $f_{\text{O,tot}}$ (top x-axis) versus temperature phase portrait and (top panel) $\langle R \rangle_{\text{part}}$ versus homopolymer loading at 60 °C for **O-42/OA20** blends.

This could be indicative of wet-brush incorporation of \mathbf{O} homopolymer into the particle cores, triggering an increase in the interfacial area per diblock chain thus requiring an increase in the particle aggregation number coupled with an increased degree of \mathbf{O} -block stretching. In contrast, higher α -blends ($\alpha = 1.0$, 0.80), which are expected to display dry-brush homopolymer incorporation into the particle cores, only reach maximum $\langle R \rangle_{\text{part}} \approx 9$ nm. Finally, the $\alpha = 0.23$ blends exhibit comparable particle sizes to those of $\alpha = 0.42$ blends (11 nm in \mathbf{O} -23/ \mathbf{O} A20), yet the increase in $\langle R \rangle_{\text{part}}$ is much more gradual with increasing \mathbf{O} addition. The latter observation suggests that these blends do not strictly follow the expected trends for wet brush homopolymer incorporation. They likely represent something more akin to slightly selective solvation (*vide infra*).

The thermal transition between pure HEXc and pure C15 upon cooling the $\phi_{O'} = 0.055$ **O-42/OA16** blend (Fig. 8A) enables a comparison between the particle sizes in these phases. The small HEXc/C15 coexistence window for the $\phi_{O'} = 0.055$ blend at 70 °C displays a ratio of the C15 average particle radius $(\langle R \rangle_{\text{part}} = 8.84 \text{ nm})$ to HEXc cylinder radius $(\langle R \rangle_{\text{cyl}} = 10.9 \text{ nm})$ of 1.23. In the $\phi_{O'} = 0.031$ **O-23/OA20**

blend at 119 °C, the HEXc phase ($\langle R \rangle_{\rm cyl} = 7.99$ nm) similarly coexists with the C15 phase ($\langle R \rangle_{\rm part} = 9.72$ nm), with a 1.22-fold difference in particle radii between spheres and cylinders. The sphere-cylinder size ratio persists far beyond the onset of macrophase separation and is fully thermoreversible, as illustrated in Figure 10 for a **O-42/OA16** blend with $\phi_O = 0.32$, a homopolymer loading that exceeds the bounds of the phase portrait in Fig. 8B. Different thermal treatments of a pure PI-PLA diblock copolymer by Kim, et al. led to the formation of HEXc and C15 at the same temperature, resulting in the ratio $R_{\rm C15}/R_{\rm cyl} = 1.48$, which is notably larger than what we report here. However, this comparison ignores some significant differences, most notably that the previous work dealt with a pure diblock and was based on two very different processing histories. Thus, one or both states are likely out of equilibrium. Here, the ratios of particle and cylinder radii are drawn from coexisting phases that include **O** homopolymer, which may be distributed asymmetrically.

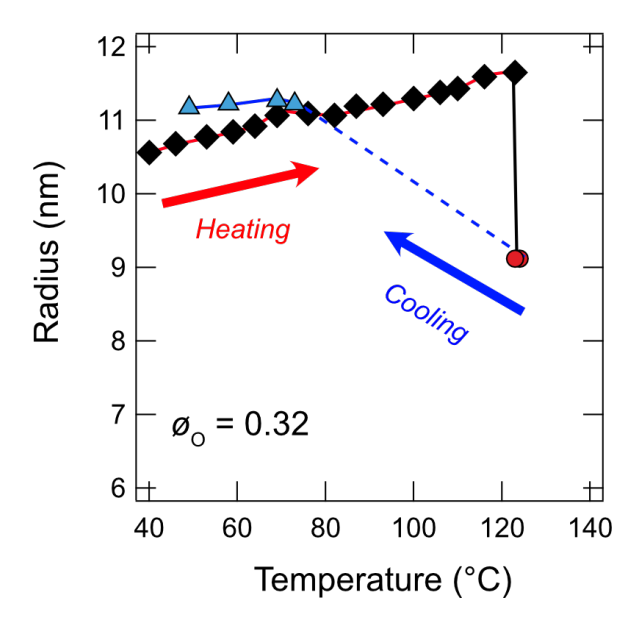


Figure 10: Particle size evolution of the **O-42/OA16** blend with $\phi_O = 0.32$ on heating then cooling. The large jump corresponds to the sphere-cylinder transition, which is fully reversible. Filled diamonds indicate LLP, blue triangles indicate C15, and red circles denote HEXc.

In summary, the **O-42**-based blends (1) recover the 'missing' wet-brush behavior by revealing sizable stability windows of HEXc, and (2) establish that even low α systems favor C15 at sufficient core homopolymer loadings. Taken together, the eight blends investigated, spanning $\alpha = 0.23, 0.42, 0.80$, and

1.00 and two diblock core-compositions $f_{\text{core}} = 0.15$, 0.16 and 0.20 provide a detailed map of the phase space made available by simple core-homopolymer diblock blends.

DISCUSSION

The experiments described herein demonstrate that adding core-homopolymer to a particle-forming diblock copolymer melt enables access to a complex particle packing phase space, which can be navigated by tuning the homopolymer length and overall f_{core} . The current work extends our earlier study on **B** particle core-forming B'/SB blends to the significantly higher conformational asymmetry (E) afforded by **OA** diblock copolymers ($\varepsilon \approx 3.5$ versus 1.7 for **SB**). In that study, dry-brush blends with $\alpha \approx 1$ stabilized only point particles, whereas wet-brush blends ($\alpha \approx 0.60$) transformed BCC phases directly into HEXc. Based on pioneering work in the 1990s, 55,57,58,69 this behavior was rationalized by the distribution of homopolymer within the melt,⁵¹ whereby $\alpha \approx 1$ homopolymer is entropically excluded from the coreblock brush. Consequently, homopolymer is localized at the centers of the particle cores, thereby preserving high intrinsic interfacial curvature associated with the diblock. By analogy, this phenomenon lies at the heart of the BCC $\rightarrow \sigma \rightarrow C14 \rightarrow C15$ phase progression in the **O-100/OA20** blends despite the larger value of ε considered here. Conversely, reducing $N_{O'}$ toward the wet-brush regime drives a more uniform distribution of homopolymer in the particle cores. Thus, the diblock chains are forced to spread out at the interface, flattening interfacial curvature and facilitating a transition to cylinders as found in the O-42/OA blends (Fig. 9). This result concurs with that found in related B'/SB blends and conforms to recent theoretical predictions based on SCFT.^{59,60} However, close inspection of the **O-42**, **O-23**, and **O-**80 blends with OA indicates that the high conformational asymmetry of the OA diblock ($\varepsilon = 3.5$) relative to the previously studied SB system ($\varepsilon = 1.7$) counteracts these effects, leading to widespread particlephase stability even in wet-brush blends. This increase in ε reinforces curvature toward the minority $\mathbf{0}$ domain, suppressing the expected particle-cylinder transition with increasing core volume fraction upon wet brush (low α) homopolymer addition. The prevalence of wet-brush particle phases in O'/OA blends allowed us to examine the dependence of particle packing symmetry on α .

The differences in particle packing between the OA blends containing O-23, O-42, O-80, and O-100 can be largely rationalized in terms of the distribution of homopolymer within the OA microstructure. Current explanations of FK and DDQC phase formation in diblock copolymer melts rely on particle shape optimization. These diblock particles are self-assembled incompressible liquids, which must fill space at constant density. This requires nominally spherical particles to facet into coordination polyhedra known as Wigner-Seitz (WS) cells as a function of local lattice symmetry. Whereas the high symmetry BCC, HCP, and FCC phases contain a single particle shape and size, FK phases have multiple particle shapes and sizes representing a mixture of 12-, 14-, 15- and 16-fold coordination polyhedra (referred to as Z12, Z14, Z15, Z16 in Figure 1C). The BCC $\rightarrow \sigma \rightarrow$ C14 \rightarrow C15 phase progression found in the **O-100/OA20** blends (Fig. 2) and previously reported B'/SB blends, 51,59,60 with increasing core-homopolymer loading at $\alpha \approx 1$ reflects increasing volume asymmetry between particles in a given phase. Recent geometric calculations suggest that the volume dispersity in FK phases is associated with an overall reduction in interfacial area. ^{27,30} In bulk diblock copolymer melts, this volume dispersity is constrained by the entropic cost of chain stretching while accommodating multiple particle sizes. This results in the prevalence of the σ phase, characterized by Z12, Z14 and Z15 particles, where the coordination polyhedra volume ratio $V_{Z15}/V_{Z12} = 1.34$ according to the unconstrained diblock foam model of Reddy et al.²⁷ However, homopolymers localize at the particle centers in dry-brush blends, thus mitigating the packing frustration associated with the more highly volume disperse C14 and C15 phases, which contain Z12 and Z16 polyhedra with $V_{Z16}/V_{Z12} = 1.47.^{27}$ Therefore, homopolymer addition furnishes an additional degree of freedom that enables their formation as equilibrium structures. 51,59,60,65

Reducing the diblock copolymer composition from $f_0 = 0.20$ to 0.15 in blends containing **O-100** truncates the homopolymer loading-dependent phase sequence from BCC $\rightarrow \sigma \rightarrow C14 \rightarrow C15 \rightarrow 2$ -phase (Fig. 2) to BCC $\rightarrow \sigma \rightarrow C14 \rightarrow 2$ -phase (Fig. 3). These findings add to a growing body of empirical evidence demonstrating a preference for C14 over σ on forming FK phases at 'low' overall particle core fractions.^{25,70} It is difficult to comment on the robustness of these results since the C14 and C15 phases

are nearly energetically degenerate, comprised of alternative stackings of equivalent particle-layers, akin to the relationship between HCP (ABABA...) and FCC (ABCABC...). Indeed, repeating the **O-80** blend experiment with **OA20** resulted in the formation of C14/C15 coexistence proximal to the onset of macrophase separation (Fig. 6), consistent with the small free energy differences between the C14 and C15 packings. In fact, even the 'pure' C15 SAXS patterns of Fig. 2A shows some degree of peak asymmetry, which may be associated with stacking faults or some degree of C14 coexistence.

Intermediate homopolymer loadings involving the **OA15** diblock copolymer revealed a surprising deviation from the **O-100/OA15** blend phase behavior, with the formation of an HCP phase in **O-80/OA15** (Fig. 4B) and **O-23/OA15** (Fig. 4A) blends. Slightly increasing the diblock composition from $f_0 = 0.15$ to 0.16 eliminated HCP, underscoring the remarkable sensitivity of these systems to minor diblock composition changes. We note that the difference in composition between OA15 and OA16 is $\Delta f \approx 0.01 \pm 0.02$ within experimental uncertainty, while the BCC $\rightarrow \sigma \rightarrow C14 \rightarrow C15$ phase progression of **O-100/OA20** blends occurs over a composition span $\Delta f \approx 5 \pm 2$ %.

Within the particle shape-optimization framework, packing frustration and interfacial area minimization render close packed structures (e.g., FCC and HCP) unstable with respect to BCC and the FK phases. This is geometrically illustrated in Figure 11, in which the dimensionless interfacial area and chain stretching are plotted for each lattice observed in this work. Dimensionless interfacial area represents the average WS cell surface area per unit volume averaged over the particles in a unit cell, normalized by the result for the BCC structure. This quantity, multiplied by the surface tension, is proportional to the enthalpy of a particular particle packing assuming a perfectly faceted particle core/corona (O/A) interface. The dimensionless chain stretching for a particular particle is calculated as the second-moment of the volume of the WS cell, which is proportional to the mean-squared distance between any point in the WS cell and its center per Reddy *et al.*²⁷ This quantity quantifies variations in coil length required to fill aspherical particle shapes and is averaged over the all the particles in a unit cell. Note these quantities are scaled by powers of 2/3 (area) and 1/3 (stretching) in Figure 11 on account of

their relative contributions to the overall free energy in the diblock foam model,²⁷ which enables direct comparisons.

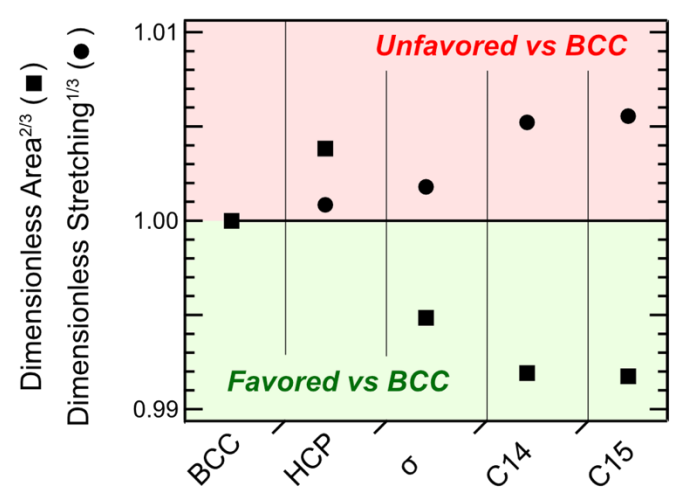


Figure 11: Comparison of the dimensionless interfacial area and chain stretching associated with the particle shapes prescribed by the different lattices identified in this work. Data for BCC, σ , C14, and C15 are results reported by Reddy *et al.*,²⁷ from which particle sizes are reported in this work. All data are normalized to the values of the BCC phase.

Whereas introducing particle size asymmetry (e.g., FK σ, C14 and C15 phases) increases the chain stretching, this energy penalty is balanced by reduction of the net interfacial area afforded by these lattices. Accordingly, Figure 11 depicts a key geometric trend: in cases where chain stretching minimization is less important, e.g., is alleviated through particle core-localized homopolymer, area minimization dominates the overall free energy to form volume-disperse surface-minimizing C14 and C15 phase.

Conventionally, close-packed lattices rarely appear in diblocks, and then only at low segregation strengths, ¹⁸ where free diblock chains in the matrix screen interparticle repulsions that drive faceting and shape optimization. Consequently, the system adopts a close-packed lattice of globally high lattice entropy. Similar effects have been achieved with matrix-homopolymer blending^{20,71} and in bidisperse diblock/diblock blends. ⁴⁶ However, because the HCP phase appears in this work at lower temperatures or higher segregations than BCC (Fig. 4B) or σ (**O-23/OA20** blends in Fig. 4A), this rationalization seems unlikely.

We propose that this phenomenon stems from a reduction in packing frustration afforded by the corehomopolymer. Indeed, this leads to widespread FK phase formation at sufficient overall core-fractions. However, if the particle cores are small enough relative to the corona size, the interfacial shape will be decoupled from the lattice symmetry and may allow formation of an entropy maximizing close-packed structure. This explains the prevalence of HCP in OA15 blends, with relatively smaller particle cores, and the lack thereof in OA20 blends, with relatively larger particle cores. Our observation of an **O'/OA** blend HCP complements previous reports of block polymer HCP phases in bulk diblocks^{18,19} and triblocks.^{72,73} Each of these cases identify the buildup of free chains (or chain ends) in the matrix, similar to the blend cases discussed above, screening interactions between micelles, enabling the formation of HCP over BCC. The apparent stabilization of HCP with core-homopolymer identified herein seemly represents an alternative mechanism. More work is required to establish precise design rules for stabilizing close packed phases such as HCP in micellar block copolymer melts. An analogous phenomenon has been observed in oil-swollen surfactant micelles.⁸

Blends containing **O-23**, the smallest homopolymer, did not produce the Laves C14 or C15 phases obtained in dry brush blends, nor a transition to cylinders characteristic of conventional wet-brush systems. Instead, the O-23 blends with OA15, OA16 and OA20 all showed a strong propensity for σ phase formation at homopolymer loadings exceeding those leading to BCC (or HCP in the case of **OA15**). With a more uniform homopolymer distribution in the particle cores relative to dry-brush blends (Fig. 12B), and high conformational asymmetry suppressing the onset of cylinders (Fig. 12C), the diblock must still stretch to fill the entire particle core (Fig. 12D). This space filling condition constrains the allowed variations in particle volumes, ΔV , resulting in a powerful preference for σ akin to that seen in neat diblocks. In fact, O-23/OA15 and O-23/OA16 blends each showed macrophase separation from σ. Suggestions of a transition towards Laves phases emerge only in the O-23/OA20 blends (80 and 69 °C SAXS patterns in Figure 8) at the highest homopolymer loadings. Here, it is possible that once the core O-block is fully swollen with homopolymer, particles continue to swell by forming pure homopolymer cores as illustrated in Figure 12F to allow a greater ΔV that enables C14/C15 formation. This argument is supported by the observation of a C15 phase in a ternary A'/AB/B' blend with minority diblock fraction,⁵⁴ with wet brush conditions in both the core and corona.

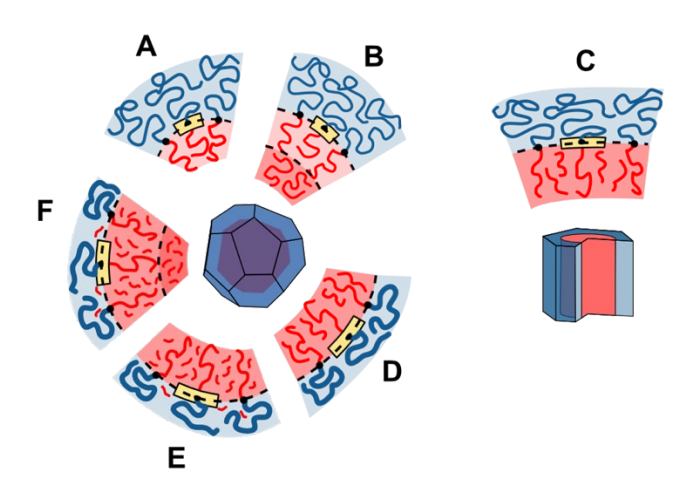


Figure 12: The different core-homopolymer swelling mechanisms associated with either stabilizing (A-E) or destabilizing (C) particle-based diblock copolymer morphologies. (A) Represents a neat compositionally asymmetric diblock copolymer, (B) depicts a dry-brush diblock/homopolymer blend, (C) illustrates a wet-brush diblock/homopolymer blend, and (D-F) show wet-brush diblock/homopolymer blends with conformationally asymmetric diblock copolymers. The yellow boxes at each interface represent a qualitative measure of the interfacial area per chain.

Alternatively, the absence of Laves phase formation in the O-23 blends could also derive from partial mixing of the low molecular weight additive with the corona blocks in a manner that effectively reduces the net core volume fraction, f_{core} . The fact that cylinders do not appear until $\phi_{\text{O'}} \ge 0.25$ or $f_{\text{core,tot}} \ge 0.40$ in the O-23/OA20 blends, and only at elevated temperatures, suggests that homopolymer does not reside solely in the particle cores; the expected sphere-cylinder order-order transition (OOT) is $0.25 < f \le 0.28$ for undiluted OA diblock melts. This possibility is supported by the fact that the particle radii in **O**-23/OA20 blends exceed 10 nm, whereas all of the other blends saturate with $\langle R \rangle_{part} \leq 9$ nm. The low molar mass of **O-23**, which borders on being an oligomeric solvent, is consistent with this behavior. As a result, the actual overall core volume fractions of these blends are probably lower than those reported in Figure 4. However, the considerable increase in $T_{\rm ODT}$ upon adding **O-23** to **OA20** or **OA15**, closely mirroring what occurs in the O-100/OA20 and O-100/OA15 blends, argues that O-23 does not act as a common solvent for both blocks. Instead, O-23 selectively swells the particle cores. In contrast to corehomopolymer blends, corona-homopolymer blends favor increasing interfacial curvature with more wetbrush character (Figure 12E). Accordingly, this matrix homopolymer would be expected to reinforce the stability of particle phases by counteracting the reduction of interfacial curvature of the wet-brush corehomopolymer additive. Intriguingly, **O-23** based blends absorb only a finite amount of homopolymer (about 7% and 25% in OA15 and OA20, respectively), which would not be expected if solvation occurred in both domains.

Blends **O-42/OA16** and **O-42/OA20** were prepared with the intention of ensuring insolubility in the matrix A-domain while maintaining strong wet-brush swelling of the O-domains. As discussed in the context of Figure 12, this had the desired effect of driving these systems to form cylinders in a manner consistent with wet-brush behavior. However, even these blends also exhibit a transition to a Laves C15 phase at sufficient homopolymer loadings. The fact that both wet and dry brush blends ultimately favor Laves phases suggests that the precise homopolymer distribution within the particle cores is less important in dictating particle packing symmetry than the combination of core-homopolymer content and overall core-fraction. This line of reasoning is consistent with the prevalence of the σ phase and closely related DDQC in **O-23/OA20** blends (Fig. 6), where we posit that some amount of matrix-solubilization of homopolymer lowers the overall particle core volume fractions.

CONCLUSIONS

Morphological investigations of particle-forming **OA** diblock copolymers blended with core domain **O**-homopolymers demonstrates a delicate balance between the molecular weight of the homopolymer and the core-block molecular weight in the formation of a plethora of ordered Frank-Kasper (FK), Laves, and close-packed structures. In the $\alpha=1$ dry-brush limit, core swelling of **OA20** (f=0.20) with **O** homopolymer confirms the previously established sequence of phases BCC $\rightarrow \sigma \rightarrow C14 \rightarrow C15$ with increasing amounts of additive over the composition range $0 \le \phi_O \le 0.07$, followed by macroscopic phase separation on further homopolymer addition. Reducing the diblock composition to f=0.15 (**OA15**), while maintaining $\alpha=1$, results in BCC $\rightarrow C14$ ($0 \le \phi_O \le 0.055$) followed by phase separation. These results reinforce earlier findings and theoretical predictions regarding the impact of core-selective homopolymer on FK phase formation in the dry-brush limit. Reducing the homopolymer molecular weight drives it to

mix with the core blocks to form a wet brush, dramatically influencing the resulting phase behavior. At intermediate homopolymer molecular weight ($\alpha = 0.80$) and f = 0.15 (OA15), SAXS measurements revealed the sequence BCC \rightarrow HCP \rightarrow C14, followed by macrophase separation, with increasing $\phi_{O'}$. The emergence of HCP between BCC and FK phases on increasing core-fraction represents unexpected behavior, possibility revealing core-homopolymer loading of highly asymmetric diblocks as a mechanism for stabilizing close-packed diblock phases. Replacing **OA15** with **OA20** while keeping $\alpha = 0.80$ transforms the phase sequence to BCC $\rightarrow \sigma \rightarrow DDQC \rightarrow (C14/C15)$ followed by phase separation. Reducing α to 0.42 leads to the formation of HEXc in blends formed with **OA16** (f = 0.16) and **OA20**. which can be rationalized based on expansion of the interfacial area per diblock copolymer chain due to wet-brush behavior in the particle cores. Finally, experiments with **OA20** and $\alpha = 0.23$ produced seemingly puzzling results. The ordered phase window greatly widened with σ and DDQC at $0 \le \phi_{0} \le$ 0.13 and poorly defined C14/C15 at $0.13 \le \phi_{0'} \le 0.25$. Also, the associated particle radii expanded beyond what was found in any of the other blends. We interpret this behavior as evidence that the homopolymer is partially distributed in the corona portion of the morphologies as well as the particle cores, i.e., the Ohomopolymer is behaving more like a partially-selective solvent.

This study exposes remarkable sensitivities of FK (σ), Laves (C14, C15), and DDQC phases, along with the more densely packed BCC and HCP morphologies, to variations in blended homopolymer molecular weight and diblock copolymer composition. All three pure OA diblocks exhibit only BCC and disordered phases. Blending relatively small amounts of O-homopolymer drives the formation of 6 additional particle morphologies, along with hexagonally-packed cylinders. These findings provide qualitative confirmation of the phase complexity anticipated by SCFT, ^{59,60} which has demonstrated nearly degenerate free energies are associated with these myriad particle packings.

ASSOCIATED CONTENT

Supporting Information

The Supporting Information is available free of charge at: [inset url]

Experimental details and additional characterization data (PDF)

AUTHOR INFORMATION

Corresponding Authors

Mahesh K. Mahanthappa – Department of Chemical Engineering and Materials Science, University of Minnesota, Minnesota, Minnesota 55455, United States; orcid.org/0000-0002-9871-804X; Email: maheshkm@umn.edu

Frank S. Bates – Department of Chemical Engineering and Materials Science, University of Minnesota, Minnesota, Minnesota 55455, United States; orcid.org/0000-0003-3977-1278; Email: bates001@umn.edu

Authors

Andreas J. Mueller – Department of Chemical Engineering and Materials Science, University of Minnesota, Minnesota 55455, United States; orcid.org/0000-0002-4750-480X

Aaron P. Lindsay – Department of Chemical Engineering and Materials Science, University of Minnesota, Minnesota, Minnesota 55455, United States; orcid.org/0000-0003-0223-193X

Ashish P. Jayaraman – Department of Chemical Engineering and Materials Science, University of Minnesota, Minnesota 55455, United States; orcid.org/0000-0001-7071-7419

Timothy P. Lodge – Department of Chemical Engineering and Materials Science and Department of Chemistry, University of Minnesota, Minnesota, Minnesota 55455, United States;

Steven Weigand – DND-CAT Synchrotron Research Center, Northwestern University, Argonne, Illinois 60439, United States

Notes

The authors declare no competing financial interest.

ACKNOWLEDGMENTS

Financial support for this work was provided by the U.S. National Science Foundation under grants DMR-1801993 (A.J.M., F.S.B.) and CHE-1807330 (A.J., M.K.M.), and through an NSF Graduate Research Fellowship under Grant No. 00039202 (A.P.L.). SAXS experiments were carried out at Sector 12 and Sector 5 of the Advanced Photon Source (APS). The Sector 5 DuPont-Northwestern-Dow Collaborative Access Team (DND-CAT) is supported by E.I. DuPont de Nemours & Co., the Dow Chemical Company, and Northwestern University. Use of the APS, an Office of Science User Facility operated for the U.S. Department of Energy (DOE) Office of Science by Argonne National Laboratory, was supported by the U.S. DOE under Contract No. DE-AC02-06CH11357. Parts of this work, including lab source SAXS analyses, were carried out in the Characterization Facility at the University of Minnesota, which receives partial support from NSF through the UMN MRSEC (DMR-2011401). ¹H NMR spectra used in this study were collected on a Bruker Avance II HD 400 MHz spectrometer purchased by the Office of the Vice President of Research, the College of Science of and Engineering, and the Department of Chemistry at the University of Minnesota. MALDI-ToF data were obtained at the Mass Spectroscopy Laboratory located in the Chemistry Department at the University of Minnesota, supported by the Office of the Vice President of Research, the College of Science and Engineering, and the Department of Chemistry at the University of Minnesota, as well as The National Science Foundation (NSF CHE-1336940).

REFERENCES

- (1) Frank, F. C.; Kasper, J. S. Complex Alloy Structures Regarded as Sphere Packings. II. Analysis and Classification of Representative Structures. *Acta Crystallogr.* **1959**, *12*, 483–499.
- (2) Frank, F. C.; Kasper, J. S. Complex Alloy Structures Regarded as Sphere Packings. I. Definitions and Basic Principles. *Acta Crystallogr.* **1958**, *11*, 184–190.
- (3) Levine, D.; Steinhardt, P. J. Quasicrystals: A New Class of Ordered Structures. *Phys. Rev. Lett.* **1984**, *53*, 2477–2480.
- (4) Luzzati, V.; Vargas, R.; Gulik, A.; Mariani, P.; Seddon, J. M.; Rivas, E. Lipid Polymorphism: A Correction. The Structure of the Cubic Phase of Extinction Symbol Fd--Consists of Two Types of Disjointed Reverse Micelles Embedded in a Three-Dimensional Hydrocarbon Matrix.

 Biochemistry 1992, 31, 279–285.
- (5) Seddon, J. M.; Zeb, N.; Templer, R. H.; McElhaney, R. N.; Mannock, D. A. An Fd3m Lyotropic Cubic Phase in a Binary Glycolipid/ Water System. *Langmuir* **1996**, *12*, 5250–5253.
- (6) Kim, S. A.; Jeong, K.-J.; Yethiraj, A.; Mahanthappa, M. K. Low-Symmetry Sphere Packings of Simple Surfactant Micelles Induced by Ionic Sphericity. *Proc. Natl. Acad. Sci.* **2017**, *114*, 4072–4077.
- (7) Jayaraman, A.; Mahanthappa, M. K. Counterion-Dependent Access to Low-Symmetry Lyotropic Sphere Packings of Ionic Surfactant Micelles. *Langmuir* **2018**, *34*, 2290–2301.
- (8) Jayaraman, A.; Baez-Cotto, C. M.; Mann, T. J.; Mahanthappa, M. K. Dodecagonal Quasicrystals of Oil-Swollen Ionic Surfactant Micelles. *Proc. Natl. Acad. Sci. U. S. A.* **2021**, *118*, 2290–2301.
- (9) Ungar, G.; Liu, Y.; Zeng, X.; Percec, V.; Cho, W. D. Giant Supramolecular Liquid Crystal Lattice. *Science*. **2003**, *299*, 1208–1211.
- (10) Zeng, X.; Ungar, G.; Liu, Y.; Percec, V.; Dulcey, A. E.; Hobbs, J. K. Supramolecular Dendritic Liquid Quasicrystals. *Nature* **2004**, *428*, 157–160.
- (11) Percec, V.; Peterca, M.; Tsuda, Y.; Rosen, B. M.; Uchida, S.; Imam, M. R.; Ungar, G.; Heiney, P.

- A. Elucidating the Structure of the Pm3n Cubic Phase of Supramolecular Dendrimers through the Modification of Their Aliphatic to Aromatic Volume Ratio. *Chem. Eur J.* **2009**, *15*, 8994–9004.
- (12) Huang, M.; Hsu, C. H.; Wang, J.; Mei, S.; Dong, X.; Li, Y.; Li, M.; Liu, H.; Zhang, W.; Aida, T.; Zhang, W. Bin; Yue, K.; Cheng, S. Z. D. Selective Assemblies of Giant Tetrahedra via Precisely Controlled Positional Interactions. *Science*. **2015**, *348*, 424–428.
- (13) Su, Z.; Hsu, C.; Gong, Z.; Feng, X.; Huang, J.; Zhang, R.; Wang, Y.; Mao, J.; Wesdemiotis, C.; Li, T.; Seifert, S.; Zhang, W.; Aida, T.; Huang, M.; Cheng, S. Z. D. Identification of a Frank–Kasper Z Phase from Shape Amphiphile Self-Assembly. *Nat. Chem.* **2019**, *11*, 899–905.
- Yue, K.; Huang, M.; Marson, R. L.; Hec, J.; Huang, J.; Zhou, Z.; Wang, J.; Liu, C.; Yan, X.; Wu, K.; Guo, Z.; Liu, H.; Zhang, W.; Ni, P.; Wesdemiotis, C.; Zhang, W. Bin; Glotzer, S. C.; Cheng, S. Z. D. Geometry Induced Sequence of Nanoscale Frank-Kasper and Quasicrystal Mesophases in Giant Surfactants. *Proc. Natl. Acad. Sci. U. S. A.* 2016, *113*, 14195–14200.
- (15) Liu, Y.; Liu, T.; Yan, X. Y.; Guo, Q. Y.; Lei, H.; Huang, Z.; Zhang, R.; Wang, Y.; Wang, J.; Liu, F.; Bian, F. G.; Meijer, E. W.; Aida, T.; Huang, M.; Cheng, S. Z. D. Expanding Quasiperiodicity in Soft Matter: Supramolecular Decagonal Quasicrystals by Binary Giant Molecule Blends. *Proc. Natl. Acad. Sci. U. S. A.* **2022**, *119*, e2115304119.
- (16) Chanpuriya, S.; Kim, K.; Zhang, J.; Lee, S.; Arora, A.; Dorfman, K. D.; Delaney, K. T.; Fredrickson, G. H.; Bates, F. S. Cornucopia of Nanoscale Ordered Phases in Sphere-Forming Tetrablock Terpolymers. *ACS Nano* **2016**, *10*, 4961–4972.
- (17) Barbon, S. M.; Song, J. A.; Chen, D.; Zhang, C.; Lequieu, J.; Delaney, K. T.; Anastasaki, A.; Rolland, M.; Fredrickson, G. H.; Bates, M. W.; Hawker, C. J.; Bates, C. M. Architecture Effects in Complex Spherical Assemblies of (AB)n-Type Block Copolymers. *ACS Macro Lett.* **2020**, *9*, 1745–1752.
- (18) Huang, Y. Y.; Hsu, J. Y.; Chen, H. L.; Hashimoto, T. Existence of Fcc-Packed Spherical Micelles in Diblock Copolymer Melt. *Macromolecules* **2007**, *40*, 406–409.
- (19) Hsu, N. W.; Nouri, B.; Chen, L. T.; Chen, H. L. Hexagonal Close-Packed Sphere Phase of

- Conformationally Symmetric Block Copolymer. *Macromolecules* **2020**, *53*, 9665–9675.
- (20) Huang, Y.-Y.; Chen, H.-L.; Hashimoto, T. Face-Centered Cubic Lattice of Spherical Micelles in Block Copolymer/Homopolymer Blends. *Macromolecules* **2003**, *36*, 764–770.
- (21) Takenaka, M.; Wakada, T.; Akasaka, S.; Nishitsuji, S.; Saijo, K.; Shimizu, H.; Kim, M. I.; Hasegawa, H. Orthorhombic Fddd Network in Diblock Copolymer Melts. *Macromolecules* **2007**, *40*, 4399–4402.
- (22) Tyler, C. A.; Morse, D. C. Orthorhombic Fddd Network in Triblock and Diblock Copolymer Melts. *Phys. Rev. Lett.* **2005**, *94*, 208302.
- (23) Gillard, T. M.; Lee, S.; Bates, F. S. Dodecagonal Quasicrystalline Order in a Diblock Copolymer Melt. *Proc. Natl. Acad. Sci. U. S. A.* **2016**, *113*, 5167–5172.
- (24) Lee, S.; Bluemle, M. J.; Bates, F. S. Discovery of a Frank-Kasper σ Phase in Sphere-Forming Block Copolymer Melts. *Science*. **2010**, *330*, 349–353.
- (25) Kim, K.; Schulze, M. W.; Arora, A.; Lewis, R. M.; Hillmyer, M. A.; Dorfman, K. D.; Bates, F. S. Thermal Processing of Diblock Copolymer Melts Mimics Metallurgy. *Science*. **2017**, *356*, 520–523.
- (26) Bates, M. W.; Lequieu, J.; Barbon, S. M.; Lewis, R. M.; Delaney, K. T.; Anastasaki, A.; Hawker,
 C. J.; Fredrickson, G. H.; Bates, C. M. Stability of the A15 Phase in Diblock Copolymer Melts.
 Proc. Natl. Acad. Sci. U. S. A. 2019, 116, 13194–13199.
- (27) Reddy, A.; Buckley, M. B.; Arora, A.; Bates, F. S.; Dorfman, K. D.; Grason, G. M. Stable Frank-Kasper Phases of Self-Assembled, Soft Matter Spheres. *Proc. Natl. Acad. Sci. U. S. A.* **2018**, *115*, 10233–10238.
- (28) Grason, G. M. The Packing of Soft Materials: Molecular Asymmetry, Geometric Frustration and Optimal Lattices in Block Copolymer Melts. *Phys. Rep.* **2006**, *433*, 1–64.
- (29) Grason, G. M.; DiDonna, B. A.; Kamien, R. D. Geometric Theory of Diblock Copolymer Phases. *Phys. Rev. Lett.* **2003**, *91*, 058304.
- (30) Lee, S.; Leighton, C.; Bates, F. S. Sphericity and Symmetry Breaking in the Formation of Frank-

- Kasper Phases from One Component Materials. *Proc. Natl. Acad. Sci. U. S. A.* **2014**, *111*, 17723–17731.
- (31) Thomas, E. L.; Kinning, D. J.; Alward, D. B.; Henkee, C. S. Ordered Packing Arrangements of Spherical Micelles of Diblock Copolymers in Two and Three Dimensions. *Macromolecules* 1987, 20, 2934–2939.
- (32) Sullivan, J. M. Foams and Emulsions; Sadoc, J. F., Rivier, N., Eds.; Dordrecht, Kluwer, 1999.
- (33) Xie, N.; Li, W.; Qiu, F.; Shi, A. C. σ Phase Formed in Conformationally Asymmetric AB-Type Block Copolymers. *ACS Macro Lett.* **2014**, *3*, 909–910.
- (34) Schulze, M. W.; Lewis, R. M.; Lettow, J. H.; Hickey, R. J.; Gillard, T. M.; Hillmyer, M. A.; Bates, F. S. Conformational Asymmetry and Quasicrystal Approximants in Linear Diblock Copolymers. *Phys. Rev. Lett.* **2017**, *118*, 207801.
- (35) Vigil, D. L.; Quah, T.; Sun, D.; Delaney, K. T.; Fredrickson, G. H. Self-Consistent Field Theory Predicts Universal Phase Behavior for Linear, Comb, and Bottlebrush Diblock Copolymers.

 *Macromolecules** 2022, 55, 4237–4244.
- (36) Chang, A. B.; Bates, F. S. Impact of Architectural Asymmetry on Frank-Kasper Phase Formation in Block Polymer Melts. *ACS Nano* **2020**, *14*, 11463–11472.
- (37) Sun, Y.; Tan, R.; Ma, Z.; Gan, Z.; Li, G.; Zhou, D.; Shao, Y.; Zhang, W. Bin; Zhang, R.; Dong, X. H. Discrete Block Copolymers with Diverse Architectures: Resolving Complex Spherical Phases with One Monomer Resolution. *ACS Cent. Sci.* **2020**, *6*, 1386–1393.
- (38) Bates, M. W.; Barbon, S. M.; Levi, A. E.; Lewis, R. M.; Beech, H. K.; Vonk, K. M.; Zhang, C.; Fredrickson, G. H.; Hawker, C. J.; Bates, C. M. Synthesis and Self-Assembly of ABn Miktoarm Star Polymers. *ACS Macro Lett.* **2020**, *9*, 396–403.
- (39) Xie, N.; Li, W.; Qiu, F.; Shi, A. C. σ Phase Formed in Conformationally Asymmetric AB-Type Block Copolymers. *ACS Macro Lett.* **2014**, *3*, 909–910.
- (40) Lewis, R. M.; Arora, A.; Beech, H. K.; Lee, B.; Lindsay, A. P.; Lodge, T. P.; Dorfman, K. D.; Bates, F. S. Role of Chain Length in the Formation of Frank-Kasper Phases in Diblock

- Copolymers. Phys. Rev. Lett. 2018, 121, 208002.
- (41) Jeon, S.; Jun, T.; Jo, S.; Ahn, H.; Lee, S.; Lee, B.; Ryu, D. Y. Frank–Kasper Phases Identified in PDMS-b-PTFEA Copolymers with High Conformational Asymmetry. *Macromol. Rapid Commun.* **2019**, *40*, 1900259.
- (42) Kim, K.; Arora, A.; Lewis, R. M.; Liu, M.; Li, W.; Shi, A. C.; Dorfman, K. D.; Bates, F. S. Origins of Low-Symmetry Phases in Asymmetric Diblock Copolymer Melts. *Proc. Natl. Acad. Sci. U. S. A.* **2018**, *115*, 847–854.
- (43) Liu, M.; Qiang, Y.; Li, W.; Qiu, F.; Shi, A. C. Stabilizing the Frank-Kasper Phases via Binary Blends of AB Diblock Copolymers. *ACS Macro Lett.* **2016**, *5*, 1167–1171.
- (44) Yamamoto, K.; Takagi, H. Frank-Kasper · and A-15 Phases Formed in Symmetry and Asymmetry Block Copolymer Blend System. *Mater. Trans.* **2021**, *62*, 325–328.
- (45) Lindsay, A. P.; Lewis, R. M.; Lee, B.; Peterson, A. J.; Lodge, T. P.; Bates, F. S. A15, σ, and a Quasicrystal: Access to Complex Particle Packings via Bidisperse Diblock Copolymer Blends. *ACS Macro Lett.* **2020**, 197–203.
- (46) Lindsay, A. P.; Cheong, G. K.; Peterson, A. J.; Weigand, S.; Dorfman, K. D.; Lodge, T. P.; Bates, F. S. Complex Phase Behavior in Particle-Forming AB/AB' Diblock Copolymer Blends with Variable Core Block Lengths. *Macromolecules* 2021, 54, 7088–7101.
- (47) Takagi, H.; Yamamoto, K. Phase Boundary of Frank-Kasper σ Phase in Phase Diagrams of Binary Mixtures of Block Copolymers and Homopolymers. *Macromolecules* **2019**, *52*, 2007–2014.
- (48) Takagi, H.; Hashimoto, R.; Igarashi, N.; Kishimoto, S.; Yamamoto, K. Frank–Kasper σ Phase in Polybutadiene-Poly(ε- Caprolactone) Diblock Copolymer/Polybutadiene Blends. *J. Phys. Condens. Matter* **2017**, *29*, 204002.
- (49) Baez-Cotto, C. M.; Jackson, G. L.; Mahanthappa, M. K. Aqueous Lyotropic Mesophase Behavior of Gemini Dicarboxylate Surfactants Swollen with N-Decane. *Langmuir* **2020**, *36*, 2307–2321.
- (50) Baez-Cotto, C. M.; Mahanthappa, M. K. Micellar Mimicry of Intermetallic C14 and C15 Laves

- Phases by Aqueous Lyotropic Self-Assembly. ACS Nano 2018, 12, 3226–3234.
- (51) Mueller, A. J.; Lindsay, A. P.; Jayaraman, A.; Lodge, T. P.; Mahanthappa, M. K.; Bates, F. S. Emergence of a C15 Laves Phase in Diblock Polymer/Homopolymer Blends. ACS Macro Lett. 2020, 9, 576–582.
- Uddin, M. H.; Rodriguez, C.; Lopez-Quintela, A.; Leisner, D.; Solans, C.; Esquena, J.; Kunieda,
 H.; Graduate. Phase Behavior and Microstructure of Poly(Oxyethylene)-Poly(Dimethylsiloxane)
 Copolymer Melt. *Macromolecules* 2003, 36, 1261–1271.
- (53) Uddin, M. H.; Rodriguez, C.; Watanabe, K.; Lopez-Quintela, A.; Kato, T.; Furukawa, H.; Harashima, A.; Kunieda, H. Phase Behavoir and Formation of Reverse Cubic Phase Based Emlusion in Water/Poly(Oxyethylene) Poly(Dimethylsiloxane) Surfactants/Silicone Oil Systems. *Langmuir* 2001, 17, 5169–5175.
- (54) Xie, S.; Lindsay, A. P.; Bates, F. S.; Lodge, T. P. Formation of a C15 Laves Phase with a Giant Unit Cell in Salt-Doped A/B/AB Ternary Polymer Blends. *ACS Nano* **2020**, *14*, 13754–13764.
- (55) Winey, K. I.; Thomas, E. L.; Fetters, L. J. Swelling a Lamellar Diblock Copolymer with Homopolymer: Influences of Homopolymer Concentration and Molecular Weight.

 *Macromolecules** 1991, 24, 6182–6188.
- (56) Koizumi, S.; Hasegawa, H.; Hashimoto, T. Spatial Distribution of Homopolymers in Block Copolymer Microdomains As Observed by a Combined SANS and SAXS Method. *Macromolecules* 1994, 27, 7893–7906.
- (57) Hashimoto, T.; Tanaka, H.; Hasegawa, H. Ordered Structure in Mixtures of a Block Copolymer and Homopolymers. 2. Effects of Molecular Weights of Homopolymers. *Macromolecules* **1990**, 23, 4378–4386.
- (58) Tanaka, H.; Hascgawa, H.; Hashimoto, T. Ordered Structure in Mixtures of a Block Copolymer and Homopolymers. 1. Solubilization of Low Molecular Weight Homopolymers.

 *Macromolecules** 1991, 24, 240–251.
- (59) Cheong, G. K.; Bates, F. S.; Dorfman, K. D. Symmetry Breaking in Particle-Forming Diblock

- Polymer/Homopolymer Blends. Proc. Natl. Acad. Sci. U. S. A. 2020, 117, 16764–16769.
- (60) Xie, J.; Shi, A.-C. Formation of Complex Spherical Packing Phases in Diblock Copolymer/Homopolymer Blends. *Giant* **2021**, *5*, 100043.
- (61) Mueller, A. J.; Lindsay, A. P.; Jayaraman, A.; Lodge, T. P.; Mahanthappa, M. K.; Bates, F. S. Quasicrystals and Their Approximants in a Crystalline-Amorphous Diblock Copolymer.
 Macromolecules 2021, 54, 2647–2660.
- (62) Fetters, L. J.; Lohse, D. J.; RIchter, D.; WItten, T. A.; Zirkel, A. Connection between Polymer Molecular Weight, Density, Chain Dimensions, and Melt Viscoelastic Properties. *Macromolecules* 1994, 27, 4639–4647.
- (63) Heatley, F.; Lovell, P. A.; Yamashita, T. Chain Transfer to Polymer in Free-Radical Solution Polymerization of 2-Ethylhexyl Acrylate Studied by NMR Spectroscopy. *Macromolecules* **2001**, 34, 7636–7641.
- (64) Cavicchi, K. A.; Lodge, T. P. Domain Size Equilibration in Sphere-Forming Block Copolymers.
 J. Polym. Sci. Part B Polym. Phys. 2003, 41, 715–724.
- (65) Zhao, M.; Li, W. Laves Phases Formed in the Binary Blend of AB 4 Miktoarm Star Copolymer and A-Homopolymer. *Macromolecules* **2019**, *52*, 1832–1842.
- (66) Pujar, V. V.; Cawley, J. D. Effect of Stacking Faults on the X-Ray Diffraction Profiles of β-SiC Powders. J. Am. Ceram. Soc. 1995, 78, 774–782.
- (67) Matsen, M. W. Fast and Accurate SCFT Calculations for Periodic Block-Copolymer Morphologies Using the Spectral Method with Anderson Mixing. Eur. Phys. J. E 2009, 30, 361–369.
- (68) Matsen, M. W.; Bates, F. S. Unifying Weak- and Strong-Segregation Block Copolymer Theories.

 *Macromolecules 1996, 29, 1091–1098.
- (69) Koizumi, S.; Hasegawa, H.; Hashimoto, T. Spatial Distribution of Homopolymers in Block Copolymer Microdomains as Observed by a Combined SANS and SAXS Method. *Macromolecules* 1994, 27, 7893–7906.

- (70) Jeon, S.; Jun, T.; Jeon, H. II; Ahn, H.; Lee, S.; Lee, B.; Ryu, D. Y. Various Low-Symmetry Phases in High-χ and Conformationally Asymmetric PDMS- b-PTFEA Copolymers. *Macromolecules* 2021, 54, 9351–9360.
- (71) Chen, L. T.; Huang, Y. T.; Chen, C. Y.; Chen, M. Z.; Chen, H. L. Thermodynamically Originated Stacking Fault in the Close-Packed Structure of Block Copolymer Micelles. *Macromolecules* **2021**, *54*, 8936–8945.
- (72) Zhang, C.; Vigil, D. L.; Sun, D.; Bates, M. W.; Loman, T.; Murphy, E. A.; Barbon, S. M.; Song, J. A.; Yu, B.; Fredrickson, G. H.; Whittaker, A. K.; Hawker, C. J.; Bates, C. M. Emergence of Hexagonally Close-Packed Spheres in Linear Block Copolymer Melts. *J. Am. Chem. Soc.* 2021, 143, 14106–14114.
- (73) Wang, S.; Xie, R.; Vajjala Kesava, S.; Gomez, E. D.; Cochran, E. W.; Robertson, M. L. Close-Packed Spherical Morphology in an ABA Triblock Copolymer Aligned with Large-Amplitude Oscillatory Shear. *Macromolecules* **2016**, *49*, 4875–4888.